# Pool Boiling Heat Transfer Characteristics of Nanofluids

by

Sung Joong Kim

Submitted to the Department of Nuclear Science and Engineering in

partial fulfillment of the requirements for the Degree of

Master of Science in Nuclear Science and Engineering

At the

Massachusetts Institute of Technology

May 2007

[June 2007]



Author_____

Department of Nuclear Science and Engineering

Certified by_____

Jacopo Buongiorno, Assistant Professor of Nuclear Science and Engineering Department

Thesis Supervisor

Certified by_____

Dr. Lin-Wen Hu, Associate Director in Nuclear Reactor Laboratory

Thesis Co-Supervisor

Accepted by_____

Jeff Coderre, Assistant Professor of Nuclear Science and Engineering

Chairman, Committee for Graduate Studies

# Pool Boiling Heat Transfer Characteristics of Nanofluids

by

Sung Joong Kim

Submitted to the Department of Nuclear Science and Engineering in

partial fulfillment of the requirements for the Degree of

Master of Science in Nuclear Science and Engineering

At the

MASSACHUSETTS INSTITUTE OF TECHNOLOGY

## Abstract

Nanofluids are engineered colloidal suspensions of nanoparticles in water, and exhibit a very significant enhancement (up to 200%) of the boiling Critical Heat Flux (CHF) at modest nanoparticle concentrations (≤0.1% by volume). Since CHF is the upper limit of nucleate boiling, such enhancement offers the potential for major performance improvement in many practical applications that use nucleate boiling as their prevalent heat transfer mode. The nuclear applications considered are main reactor coolant for PWR, coolant for the Emergency Core Cooling System (ECCS) of both PWR and BWR, and coolant for in-vessel retention of the molten core during severe accidents in high-power-density LWR. To implement such applications it is necessary to understand the fundamental boiling heat transfer characteristics of nanofluids. The nanofluids considered in this study are dilute dispersions of alumina, zirconia, and silica nanoparticles in water. Several key parameters affecting heat transfer (i.e., boiling point, viscosity, thermal conductivity, and surface tension) were measured and, consistently with other nanofluid studies, were found to be similar to those of pure water. However, pool boiling experiments showed significant enhancements of CHF in the nanofluids. Scanning Electron Microscope (SEM) and Energy Dispersive Spectrometry (EDS) analyses revealed that buildup

of a porous layer of nanoparticles on the heater surface occurred during nucleate boiling. This layer significantly improves the surface wettability, as shown by measured changes in the static contact angle on the nanofluid-boiled surfaces compared with the pure-water-boiled surfaces. It is hypothesized that surface wettability improvement may be responsible for the CHF enhancement.

# ACKNOWLEDGEMENTS

This work was partially supported by AREVA (PO CP04-0217), the Idaho National Laboratory (Contract no. 063, Release 18), the Nuclear Regulatory Commission (NRC-04-02-079), the DOE Innovation in Nuclear Infrastructure and Education Program (DOE-FG07-02ID14420). The author would also like to acknowledge the financial support he received for a doctoral fellowship provided by the Koreas Science and Engineering Foundation (KOSEF) and Korean Ministry of Science and Technology (MOST). The author gratefully appreciates Prof. Jacopo Buongiorno, Dr. Lin-Wen Hu and Dr. In Cheol Bang for their invaluable suggestion/comments on this work. Mr. Roberto Rusconi is appreciated for helping the author perform the dynamic light scattering measurement. In addition, the author wants to express special thanks to Dr. Wesley C. Williams and Jeongik Lee for their supporting and rejoicing the author during lab activities. Dr. John Bernard has been mentoring and cheering the author and is gratefully appreciated. Most importantly, the author feels very thankful for being born to parents, who always loved and encouraged the author.

# TABLE OF CONTENTS


**1 INTRODUCTION ..... 14**

**2 PARATION AND CHARACTERIZATION OF NANOFLUIDS ..... 18**

2.1 PREPARATION OF DIFFERENT CONCENTRATIONS OF NANOFLUIDS ..... 18

2.2 ACIDITY (pH) MEASUREMENT ..... 21

2.3 BOILING POINT MEASUREMENT ..... 23

2.4 SURFACE TENSION MEASUREMENT ..... 28

2.5 THERMAL CONDUCTIVITY MEASURMENT ..... 31

2.6 KINEMATIC VISCOSITY MEASUREMENT ..... 36

2.7 NANOPARTICLE SIZE MEASUREMENT ..... 40

**3 POOL BOILING WIRE AND FLAT HEATER EXPERIMENT ..... 49**

3.1 CHF EXPERIMENTS WITH WIRE ..... 49

3.2 WETTABILITY EXPERIMENTS WITH FLAT HEATER ..... 55

*3.2.1 Experimental Apparatus ..... 55*

*3.2.2 Contact Angle Measurement ..... 58*

*3.2.3 Scanning Electron Microscopy Results ..... 65*

*3.2.4 Surface Profilometer Results ..... 70*

**4 DATA INTERPRETATION ..... 74**

**5 CONCLUSION AND FUTURE WORK ..... 77**

# LIST OF FIGURES


FIGURE 2-1 A SCHEMATIC OF BOILING POINT MEASUREMENT ..... 25

FIGURE 2-2 A SCHEMATIC OF SURFACE TENSION MEASUREMENT ..... 29

FIGURE 2-3 VARIATION OF SURFACE TENSION OF TESTED NANOFLUIDS ..... 30

FIGURE 2-4 A SCHEMATIC OF THERMAL CONDUCTIVITY MEASUREMENT ..... 31

FIGURE 2-5 CANNON-FENSKE CAPILLARY VISCOMETER ..... 37

FIGURE 2-6 KINEMATIC VISCOSITY OF PURE WATER AND NANOFLUIDS ..... 39

FIGURE 2-7 A SCHEMATIC OF LIGHT SCATTERING MEASUREMENT WITH A DYNAMIC MODE ..... 42

FIGURE 2-8 DLS MEASUREMENT (0.001 V% $AL_2O_3$) ..... 45

FIGURE 2-9 DLS MEASUREMENT (0.01 V% $AL_2O_3$) ..... 46

FIGURE 2-10 DLS MEASUREMENT (0.1 V% $AL_2O_3$) ..... 46

FIGURE 2-11 DLS MEASUREMENT (0.001 V% $ZRO_2$) ..... 47

FIGURE 2-12 DLS MEASUREMENT (0.01 V% $ZRO_2$) ..... 47

FIGURE 2-13 DLS MEASUREMENT (0.1 V% $ZRO_2$) ..... 48

FIGURE 2-14 DLS MEASUREMENT (0.1 V% $SIO_2$) ..... 48

FIGURE 3-1 A SCHEMATIC OF RESISTANCE HEATING WIRE POOL BOILING FACILITY ..... 50

FIGURE 3-2 CHF DATA FOR DI WATER AND ALUMINA, ZIRCONIA AND SILICA NANOFLUIDS ..... 51

FIGURE 3-3 POOL BOILING OF PURE WATER AND 0.01 V% ALUMINA NANOFLUID AT THE SAME HEAT FLUX ON THE WIRE HEATER ..... 52

FIGURE 3-4 BOILING CURVES FOR WIRE HEATER ..... 53

FIGURE 3-5 SEM IMAGES OF WIRE HEATERS TAKEN AFTER BOILING PURE WATER AND 0.01 V% ALUMINA NANOFLUID54

FIGURE 3-6 SCHEMATICS OF (A) FLAT HEATER AND (B) HEATER ASSEMBLY ..... 55

FIGURE 3-7 CONTACT ANGLE MEASUREMENT (EASYDROP CONTACT ANGLE INSTRUMENTATION BY KRÜSS) ..... 57

FIGURE 3-8 A SCHEMATIC OF STATIC CONTACT ANGLE OF LIQUID ..... 58

FIGURE 3-9 CONTACT ANGLE OF (A) DI WATER AND (B) 0.1 V% OF $AL_2O_3$ ON THE FLAT HEATER BOILED IN THE DI WATER; (C) 0.001 V% OF $ZRO_2$ ON THE BARE FLAT HEATER ..... 59

FIGURE 3-10 CONTACT ANGLE OF 0.1V% OF $AL_2O_3$ ON THE FLAT HEATER BOILED IN THE 0.1 V % $AL_2O_3$ ..... 60

FIGURE 3-11 CONTACT ANGLE OF 0.01 V% OF $AL_2O_3$ ON THE FLAT HEATER BOILED IN THE 0.01 V % $AL_2O_3$ ..... 60

FIGURE 3-12 CONTACT ANGLE OF 0.001 V% OF $AL_2O_3$ ON THE FLAT HEATER BOILED IN THE 0.001 V% $AL_2O_3$ ..... 61

FIGURE 3-13 CONTACT ANGLE OF 0.1 V% OF $ZRO_2$ ON THE FLAT HEATER BOILED IN THE 0.1 V% $ZRO_2$ ..... 61

FIGURE 3-14 CONTACT ANGLE OF 0.01 V% OF $ZRO_2$ ON THE FLAT HEATER BOILED IN THE 0.01 V% $ZRO_2$ ..... 62

FIGURE 3-15 CONTACT ANGLE OF 0.001 V% OF $ZrO_2$ ON THE FLAT HEATER BOILED IN THE 0.001 V% $ZrO_2$ ..... 62
FIGURE 3-16 CONTACT ANGLE OF 0.1 V% OF $SiO_2$ ON THE FLAT HEATER BOILED IN THE 0.1 V% $SiO_2$ ..... 63
FIGURE 3-17 CONTACT ANGLE OF 0.01 V% OF $SiO_2$ ON THE FLAT HEATER BOILED IN THE 0.01 V% $SiO_2$ ..... 63
FIGURE 3-18 CONTACT ANGLE OF 0.01 V% OF $SiO_2$ ON THE FLAT HEATER BOILED IN THE 0.01 V% $SiO_2$ ..... 64
FIGURE 3-19 SEM PICTURE OF BARE FLAT HEATER BEFORE BOILING ..... 66
FIGURE 3-20 SEM PICTURE AND EDS SPECTRUM OF FLAT HEATER BOILED IN THE DI WATER ..... 66
FIGURE 3-21 SEM PICTURE OF FLAT HEATER BOILED IN THE 0.1 V% $Al_2O_3$ ..... 66
FIGURE 3-22 SEM PICTURE AND EDS SPECTRUM OF FLAT HEATER BOILED IN THE 0.01 V% $Al_2O_3$ ..... 67
FIGURE 3-23 SEM PICTURE OF FLAT HEATER BOILED IN THE 0.001 V% $Al_2O_3$ ..... 67
FIGURE 3-24 SEM PICTURE OF FLAT HEATER BOILED IN THE 0.1 V% $ZrO_2$ ..... 67
FIGURE 3-25 SEM PICTURE AND EDS SPECTRUM OF FLAT HEATER BOILED IN THE 0.01 V% $ZrO_2$ ..... 68
FIGURE 3-26 SEM PICTURE OF FLAT HEATER BOILED IN THE 0.001 V% $ZrO_2$ ..... 68
FIGURE 3-27 SEM PICTURE OF FLAT HEATER BOILED IN THE 0.1 V% $SiO_2$ ..... 68
FIGURE 3-28 SEM PICTURE AND EDS SPECTRUM OF FLAT HEATER BOILED IN THE 0.01 V% $SiO_2$ ..... 69
FIGURE 3-29 SEM PICTURE OF FLAT HEATER BOILED IN THE 0.001 V% $SiO_2$ ..... 69
FIGURE 3-30 PROFILOMETER IMAGES OF THE FLAT HEATER SURFACE AFTER BOILING (A) DI WATER, (B) 0.01 V% ALUMINA NANOFLUID AND (C) 0.01 V% ZIRCONIA NANOFLUID. THE RMS ROUGHNESS VALUES ARE ~0.1 AND ~2 μM, RESPECTIVELY. SIMILAR RESULTS WERE OBTAINED WITH THE OTHER NANOFLUIDS. ..... 72

# LIST OF TABLES

TABLE 1 SPECIFICATIONS OF THE TESTED NANOFLUIDS ..... 18
TABLE 2 ACIDITY (PH) OF FLUIDS MEASURED AT 1 ATM 21 °C ..... 22
TABLE 3 BOILING POINT OF NANOFLUIDS AT 1 ATM ..... 26
TABLE 4 SURFACE TENSION OF PURE WATER NANOFLUIDS MEASURED IN UNIT OF MN/M AT 1 ATM AND 22 °C ..... 30
TABLE 5 THERMAL CONDUCTIVITY OF DI WATER AND NANOFLUIDS MEASURED WITH KD2 ..... 35
TABLE 6 KINEMATIC VISCOSITY OF DI WATER AND NANOFLUIDS MEASURED AT 22 °C AND 1 ATM ..... 38
TABLE 7 PARTICLE SIZE MEASURED BY DLS TECHNIQUE (N/A DENOTES THAT PARTICLE SIZE DETECTION WAS NOT VIABLE BECAUSE THE NANOFLUIDS WERE DILUTED TOO MUCH) ..... 45
TABLE 8 STATIC CONTACT ANGLES FOR DI WATER AND NANOFLUIDS ON CLEAN AND FOULED SURFACES ..... 59

# NOMENCLATURE

| | |
|---|---|
| $c$ | Specific heat, J/kg·K |
| $D$ | Diameter, m |
| $D_o$ | Mass self diffusion coefficient, $m^2$/sec |
| $Ei$ | Exponential integral function |
| $f$ | Frequency, Hz |
| $f$ | Intermediate scattering function |
| $g$ | Acceleration of gravity, m/$sec^2$ |
| $h$ | Specific enthalpy, J/kg |
| $I$ | Current, A |
| $j$ | Superficial velocity, m/sec |
| $k$ | Thermal conductivity, W/m·K |
| $k$ | Boltzmann constant, $1.3803\times10^{-23}$ J/K |
| $L$ | Wire length, m |
| $n''$ | Nucleation site density, $m^{-2}$ |
| $N$ | Microcavity density, $m^{-2}$ |
| $q$ | Scaling factor, $m^{-1}$ |
| $q'$ | Linear power, W/m |
| $q''$ | Heat flux, W/$m^2$ |
| $r$ | Roughness factor |
| $r$ | Radius, m |
| $R$ | Radius of particle, m |

| | |
|---|---|
| $R$ | Electrical resistance of wire, Ω |
| $R_o$ | Electrical resistance of wire at 100 °C, Ω |
| $\mathcal{R}$ | Radius of curvature, m |
| $S$ | Thermal activity, J/(m·K·s$^{1/2}$) |
| $t$ | Time, sec |
| $T$ | Temperature, °C |
| $T_o$ | Temperature of wire at saturation condition at 1 atm, 100 °C |
| $V$ | Voltage, V |

*Greek symbols*

| | |
|---|---|
| $\alpha$ | Temperature coefficient of resistivity, °C$^{-1}$ |
| $\alpha$ | Thermal diffusivity, $m_2$/sec |
| $\delta$ | Thickness, m |
| $\dot{\delta}$ | Growth rate, m/s |
| $\Delta r$ | Displacement of particles, m |
| $\Delta\tau$ | Time, s |
| $\gamma$ | Euler's constant |
| $\gamma$ | Surface energy, N/m |
| $\varphi$ | Nanoparticle volumetric fraction |
| $\chi$ | Nanoparticle weight fraction |
| $\kappa$ | Constant |
| $\lambda$ | Wavelength of scattered light |

| | |
|---|---|
| $\eta$ | Dynamic viscosity, kg/m·sec |
| $\theta$ | Scattered light angle, rad |
| $\theta$ | Contact angle, degree or rad |
| $\rho$ | Density, $kg/m^3$ |
| $\sigma$ | Surface tension, N/m |
| $\tau$ | Time, s |

*Subscripts*

| | |
|---|---|
| $b$ | Bubble |
| $B$ | Boltzmann |
| $c$ | Cavity |
| $cr$ | Critical |
| $d$ | Bubble departure |
| $d$ | Macrolayer dryout |
| $e$ | Equivalent |
| $f$ | Liquid phase |
| $fg$ | Liquid-to-vapor transition |
| $g$ | Vapor phase |
| $h$ | Thermal conduction medium |
| $h$ | Hovering, heater |
| $i$ | Initial |
| $m$ | Microlayer |

| | |
|---|---|
| *n* | Nanofluid |
| *p* | Nanoparticle |
| *sat* | Saturation |
| *SL* | Solid-Liquid |
| *SV* | Solid-Vapor |
| *w* | Water |
| *w* | Wall, bubble wait |

# 1 INTRODUCTION

Many important industrial applications rely on nucleate boiling, to remove high heat fluxes from a heated surface. The practical applications considered in the nuclear field are main reactor coolant for PWR, coolant for the Emergency Core Cooling System (ECCS) of both PWR and BWR, and coolant for in-vessel retention of the molten core during severe accidents in high-power-density LWR, respectively [3]. To implement such applications it is necessary to understand the fundamental boiling heat transfer characteristics of nanofluids. Needless to say, nucleate boiling is a very effective heat transfer mechanism. However it is well known that there exists a critical value of the heat flux at which nucleate boiling transitions to film boiling, a very poor heat transfer mechanism. Therefore, in most practical applications it is imperative to maintain the operating heat flux below such critical value, which is called the Critical Heat Flux (CHF). Obviously, a high value of the CHF is desirable, because, everything else being the same, the allowable power density that can be handled by a cooling system based on nucleate boiling is roughly proportional to the CHF. Therefore, an increase of the CHF can result in more compact and efficient cooling systems for the practical applications mentioned, with significant economic benefits in all these applications.

Addition of solid nanoparticles to common fluids such as water and refrigerants is an effective way to increase the CHF. The resulting colloidal suspensions are known in the literature as nanofluids [1]. Materials used for nanoparticles include chemically stable metals (e.g., gold, silver, copper), metal oxides (e.g., alumina, zirconia, silica, titania) and carbon in various forms

(e.g., diamond, graphite, carbon nanotubes, fullerene). Nanoparticles are relatively close in size to the molecules of the base fluid, and thus, if properly prepared, can realize very stable suspensions with little erosion and gravitational deposition over long periods of time. As such, nanofluids lend themselves well to 'real world' applications, contrary to the milli- and micro-size particle slurries explored in the past, which quickly settle and often clog the flow channels.

As of today (5/07), over ten studies of CHF and nucleate boiling in nanofluids have been reported in the literature [4-16]. The findings can be summarized as follows:

- Significant CHF enhancement (up to 200%) occurs with various nanoparticle materials, including silicon, aluminum and titanium oxides.
- The CHF enhancement occurs at relatively low nanoparticle concentrations, typically less than 0.1% by volume.
- During nucleate boiling some nanoparticles precipitate on the surface and form a layer whose morphology depends on the nanoparticle materials.
- Some studies report no change of heat transfer in the nucleate boiling regime [4,6], some report heat transfer deterioration [5,10,15] and others heat transfer enhancement [7,12,16].

Researchers have carefully reported the experimental data, but they have made few attempts at and little progress in explaining the CHF enhancement mechanism. The main objective of

this study is to start developing an insight of the CHF enhancement mechanism in nanofluids. The structure of the thesis is as follows. Preparation and characterization of nanofluids used in this study are described in Section 2. Description of CHF experiments with wire heaters and surface wettability experiment with flat heaters are presented in Section 3. The interpretation of the measured CHF data and wettability change in terms of the contact angle is discussed in light of the CHF theories in Section 4. The conclusion and future work are provided in Section 5.

# 2 PARATION AND CHARACTERIZATION OF NANOFLUIDS

## 2.1 PREPARATION OF DIFFERENT CONCENTRATIONS OF NANOFLUIDS

The specifications of the tested nanofluids were obtained from vendors and are shown in Table 1. Four nanofluids have been tested in the current study, in which the alumina, zirconia, and silica nanoparticles were dispersed well in the base water. Since the diamond nanoparticles were purchased in the form of powder, however, they were not dispersed perfectly. Thus, the nanofluid with diamond nanoparticles had to be ultrasonicated enough to maintain the particles dispersed before each test.

Table 1 Specifications of the tested nanofluids

| Nanoparticles materials | $Al_2O_3$ | $ZrO_2$ | $SiO_2$ | C (diamond)* |
|---|---|---|---|---|
| Vendor | Sigma-Aldrich | Sigma-Aldrich | Applied Nanoworks | Sigma-Aldrich |
| As-purchased weight percent (wt%) | 10 | 10 | 10 | 99.5 |
| Particle size (nm) | < 20 nm | < 20 nm | < 10 nm | 3.2 nm |
| Particle density (g/mL) | 3.90 | 5.75 | 3.20 | 3.52 |
| Transparency | Opaque | Opaque | Transparent | Opaque |

* Obtained as nanoparticle powder.

The nanofluids were purchased from several vendors and were rated by weight percent (wt%). Thus, it is necessary to prepare the nanofluids to obtain different concentrations of nanoparticles in volume percent (v%). Since very dilute nanofluids are expected to be implemented in the nuclear applications, it is necessary to add a suitable amount of de-ionized

(DI) water into the initial high-concentration nanofluids. For example, in order to make $\varphi$ v% nanofluid from $a$ mL of $\chi$ wt% nanofluid, one needs to determine how much DI water should be added. When the $a$ mL of $\chi$ wt% nanofluid is said to contain $b$ mL of nanopowder of density $\rho_p$ g/mL and $c$ mL of DI water of density $\rho_f$ g/mL, the required amount of DI water, d mL, to make $\varphi$ v% nanofluid can be calculated by means of the following equations:

$$a = b + c \tag{2-1}$$

$$\chi\, wt\% = \frac{b\rho_p}{b\rho_p + c\rho_f} \times 100 \tag{2-2}$$

$$\varphi\, v\% = \frac{b}{b + c + d} \times 100 \tag{2-3}$$

Because the quantity of $b$ and $c$ are not usually known, those variables need to be eliminated. Finally the required amount of water $d$ can be expressed in terms of $a$, $\chi$, $\varphi$, $\rho_p$, and $\rho_f$, and an expression obtained which may be applied to the preparation of any nanofluid.

$$d = a\frac{\frac{1-\varphi}{\varphi} - \frac{1-\chi}{\chi}\cdot\frac{\rho_p}{\rho_f}}{1 + \frac{1-\chi}{\chi}\cdot\frac{\rho_p}{\rho_f}} \tag{2-4}$$

Based on the Eq. (2-4), in order to make 0.1 v% alumina from 1 mL of 10 wt% alumina, 26.7

mL of DI water has to be added, in which the alumina nanoparticles is assumed to have the density of 3.9 g/mL. The DI water density is 1.0 g/mL at room temperature.

It is also necessary to investigate the density change of nanofluid compared to that of DI water because any change in the thermal and transport properties can affect the overall boiling heat transfer characteristics. Since this study is mostly focused on the use of very low concentrations of nanoparticles dispersed in base water, the density is also expected to differ negligibly from that of water. In fact, the volume-averaged nanofluid density becomes very useful when it is used in any heat transfer calculation. The nanofluid density can be calculated as $\rho_p\varphi + \rho_f(1-\varphi)$, where $\varphi$ is the nanoparticle volume fraction. For example, for $\varphi$ ~0.1 v%, $\rho_p \sim 4$ g/cm$^3$ and $\rho_f \sim 1$ g/cm$^3$ the nanofluid density deviation from DI water is expected to be only 0.3 %. Assuming that the nanoparticles are as volatile as the water molecules, the density of the nanofluid vapor can be calculated as $\rho_g[\rho_p\varphi + \rho_f(1-\varphi)] / [\rho_g\varphi + \rho_f(1-\varphi)]$, which gives deviations from the pure water vapor density of the order of 0.4 % at the conditions of interest. In reality the deviation will be even smaller because the nanoparticles are less volatile than the water molecules.

## 2.2 ACIDITY (pH) MEASUREMENT

The as-purchased nanofluids of alumina and zirconia are acidic while the silica nanofluids are basic. After dilution with DI water the pH was measured using both paper and digital pH meters. This measurement is important in verifying the stability of the nanofluids because the particles can agglomerate depending on the particle surface charge. The agglomeration can be controlled by the chemical state of nanofluid, especially pH.

It is necessary to mention the effect of carbon dioxide dissolution into the nanofluids. The pH measurement is very sensitive when it comes to the measurement of water due to the fact that it contains abundant interchangeable cations and anions. The sensitivity increases when the fluid is exposed to carbon dioxide, naturally present in the air. In essence, an appropriate calibration of electrodes with different buffer solutions that can cover up the expected values of test fluids is essential to guarantee the right values. Also, careful cleaning of the electrodes after each test plays an important role in improving the accuracy of the results.

The results of the acidity measurement are reported in Table 2. The result shows that the pH of DI water used for dilution in the current study is identical to the nominal equilibrium pH of 5.7, which is known to be the value at normal atmospheric conditions with the presence of carbonic acid. This result seems to be reasonable in that the DI water may get slightly acidic when it is exposed to the ambient air.

Table 2 Acidity (pH) of fluids measured at 1 atm 21 °C

| | DI water | Tap water | $Al_2O_3$ | | | $ZrO_2$ | | | $SiO_2$ | | |
|---|---|---|---|---|---|---|---|---|---|---|---|
| Nanoparticle concentration (v%) | 0 | 0 | 0.1 | 0.01 | 0.001 | 0.1 | 0.01 | 0.001 | 0.1 | 0.01 | 0.001 |
| Paper pH meter | 5-6 | 8-9 | 4-5 | 4-5 | 5 | 3-4 | 4-5 | 4-5 | 9-10 | 8 | 7 |
| pH meter-PH212 | 5.7 | 8.9 | 4.4 | 4.5 | 5.2 | 3.45 | 4.12 | 5.16 | 9.28 | 8.3 | 7.08 |

## 2.3 BOILING POINT MEASUREMENT

The boiling point of nanofluids was investigated experimentally, because the addition of nanoparticles might affect the vapor pressure, which would change the boiling point. From the molecular point of view, the boiling point can be defined in terms of the vapor pressure of the solvent. It is the temperature that at which the vapor pressure of the liquid or solvent in a solution is equal to the external pressure. Raoult's Law [17] suggests that increasing the solute in a solution will depress the vapor pressure. This would result in having the temperature to increase even higher so that the depressed vapor pressure might become equal to the external pressure. Thus, the boiling point might be expected to be elevated when solute is increased in a solution.

At this point, it is useful to look into the nature of boiling point. The boiling point is thermodynamically related to the evaporation and condensation rate associated with the osmotic pressure generated by the solute. Whenever molecules evaporate from a liquid, the boundary layer between the liquid and vapor will move. When the liquid contains a non-volatile solute, the moving boundary layer will transfer energy to the solute molecules. This energy is included in the evaporation process, and hence, it will affect the vapor pressure and boiling temperature of a solution. In this case, the moving boundary layer works against the osmotic pressure generated by the solute.

What is addressed so far stems from the molecular size of the solute. Thus, it may be

worthwhile to question whether the nano-size solute in the pure water solvent can affect the boiling point. The first insight in using the nanofluids was that the water-based nanofluids provided by commercial vendors may exhibit the different boiling points because the vendors are likely to put certain additives to get the nanoparticles dispersed in the fluids. For example, an electrolytic solution of nitric acid can be added in the nanofluid to prevent the nanoparticles from settling down. This may lead to the elevation of boiling point. Because the effect of nanoparticles on boiling point is hard to predict a priori, the boiling point of promising nanofluids was determined experimentally.

The primary objective is to compare the boiling point of nanofluids to that of pure water. The experimental schematic is shown in Fig. 2-1. A 50 mL beaker containing the test fluid is placed onto the stirring hot plate. A K-type thermocouple is immersed in the test fluid until the sheath end reaches the middle of the fluid. After each test, the sheath end was cleaned out by acetone to remove any possible deposition of nanoparticles. The stirring plate is heated up gradually with a rotating magnet stick. The temperature is read throughout the thermocouples in conjunction with HP3852 data acquisition system. The boiling point was determined as the temperature at which the slope of temperature vs time curve goes to zero. The uncertainty of the thermocouple provided by vendor is within $\pm 1.1$ °C. The K-type thermocouple could work in the current measurement because the main interest is to see the relative change of the boiling point, not the absolute temperature.

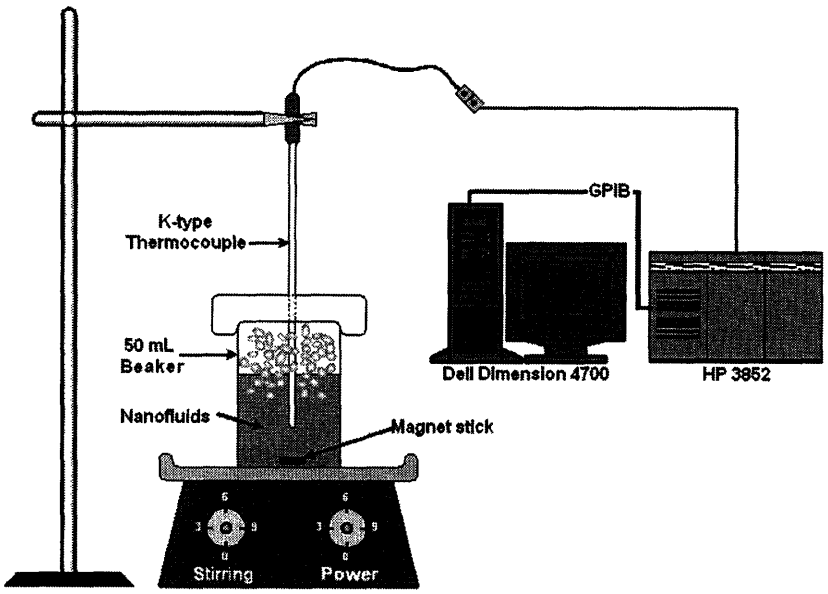


Figure 2-1 A schematic of boiling point measurement

The test results are summarized in Table 3, where it can be seen that the boiling temperatures do not vary significantly. This leads to the conclusion that the presence of nanoparticles does not affect the vapor pressure of nanofluids. This result is sensible as the Materials Safety Data Sheet (MSDS) provided by the vendors reports only nanoparticles and water as the constituents of the nanofluids.

Table 3 Boiling point of nanofluids at 1 atm

| Fluid | Nanoparticle concentration (v%) | Boiling point (°C) | $T_{f,n}$-$T_{f,w}$ (°C) |
|---|---|---|---|
| DI water | 0 | 100.6 | 0.0 |
| $Al_2O_3$ | 1.0 | 100.7 | 0.1 |
| | 0.1 | 100.8 | 0.2 |
| | 0.01 | 100.8 | 0.2 |
| $ZrO_2$ | 1.0 | 100.7 | 0.1 |
| | 0.1 | 100.1 | -0.5 |
| | 0.01 | 100.4 | -0.2 |
| $SiO_2$ | 1.0 | 100.9 | 0.3 |
| | 0.1 | 100.9 | 0.3 |
| | 0.01 | 101.0 | 0.4 |
| C (diamond) | 1.0 | 101.1 | 0.5 |
| | 0.1 | 101.0 | 0.4 |
| | 0.01 | 101.0 | 0.4 |

In summary, vapor pressure information is of importance for two-phase heat transfer studies. The vapor pressure change for our nanofluids (i.e., alumina, zirconia, silica, and diamond dispersed in water) has been studied via measurement of the relative boiling point change. The main findings are as follows:

- The boiling point of dilute nanofluids (≤1.0 v%) shows no significant change relative to that of water. This, in turn, shows that the existence of nano-size particles does not affect the vapor pressure change.
- In purchasing nanofluids from vendors, it is of importance to ascertain the possible addition of surface agents to stabilize the nanoparticles suspension. Without the

addition of specific surfactants, the vapor pressure effect could be insignificant.

## 2.4 SURFACE TENSION MEASUREMENT

Surface tension is defined as the force acting over the surface of the liquid per unit length of the surface perpendicular to the force. Surface tension is an effect within the surface sublayer of a liquid that causes that layer to behave as an elastic sheet. This is the property of a liquid in contact with ambient vapor/air or liquid, respectively. Thus, it changes as the interfacial components change. The surface tension measured in this study is that of the liquid membrane of the nanofluids at the equilibrium state with ambient air. The molecules inside the liquid interact equally with other molecules, from all sides, whereas the molecules at the surface interact only with the molecules inside the liquid. Therefore the molecules exposed to the air behave differently and try to contract to the smallest possible area.

The measurement device adopted in the current study is a digital tensiometer, Sigma 703 provided by KSV Instruments LTD. A schematic diagram of measurement apparatus is given in Fig. 2-2. The measurable range is from 0 to 200 mN/m with 0.1 mN/m of accuracy, or less than 1 % at full range. Additional uncertainty can be generated by the experimental procedure, as described next. The Wilhelmy Plate method measures the force exerted by the liquid drawn when a plate is lifted through the surface of a liquid. The force is proportional to the surface tension of the liquid. In the Wilhelmy Plate method the plate is first completely immersed into the liquid and then pulled out. Hereafter, the prewetted plate is lowered to the surface until its lower edge just touches the surface. At this point the liquid "jumps" onto the edge and sides of the plate. The liquid wets the plate perimeter and exerts a force to some

maximum point which is proportional to the surface tension of the liquid. Since the procedure is entirely manual, the results may be affected by it. Following the procedure strictly is important to ensure reliable/repeatable results.

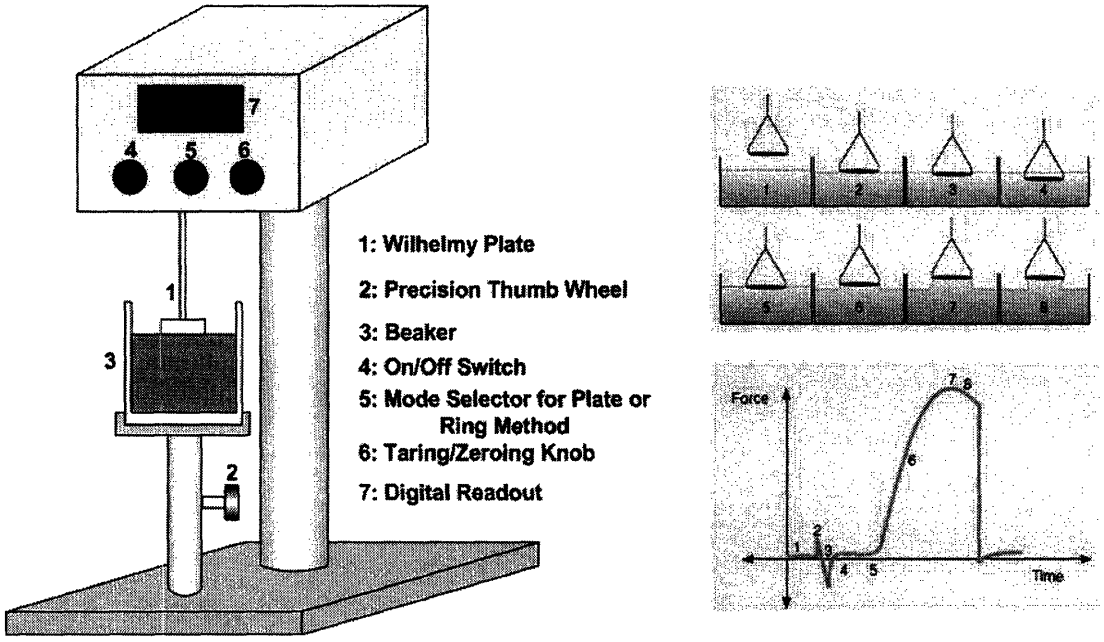


Figure 2-2 A schematic of surface tension measurement

The surface tension of various nanofluids, $\sigma_{LV}$, was measured and summarized in Table 4 and Fig. 2-3. This measurement confirms that the change of surface tension of low concentration of nanofluid compared to that of water is not significant.

Table 4 Surface tension of pure water nanofluids measured in unit of mN/m at 1 atm and 22 °C

| | Nanoparticle concentration (v%) | Test 1 | Test 2 | Test 3 | **Average** |
|---|---|---|---|---|---|
| DI Water | 0 | 72.6 | 72.8 | 72.1 | 72.5 |
| $Al_2O_3$ | 0.1 | 74.5 | 75.1 | 74.8 | 74.8 |
| | 0.01 | 73.5 | 73.5 | 73.3 | 73.4 |
| | 0.001 | 73.3 | 73.2 | 73.1 | 73.2 |
| $ZrO_2$ | 0.1 | 73.7 | 73.8 | 73.7 | 73.7 |
| | 0.01 | 73.4 | 73.4 | 73.3 | 73.4 |
| | 0.001 | 73.4 | 73.4 | 73.4 | 73.4 |
| $SiO_2$ | 0.1 | 72.4 | 72.2 | 72.6 | 72.4 |
| | 0.01 | 72.7 | 73.0 | 73.1 | 72.9 |
| | 0.001 | 73.0 | 72.9 | 73.0 | 73.0 |

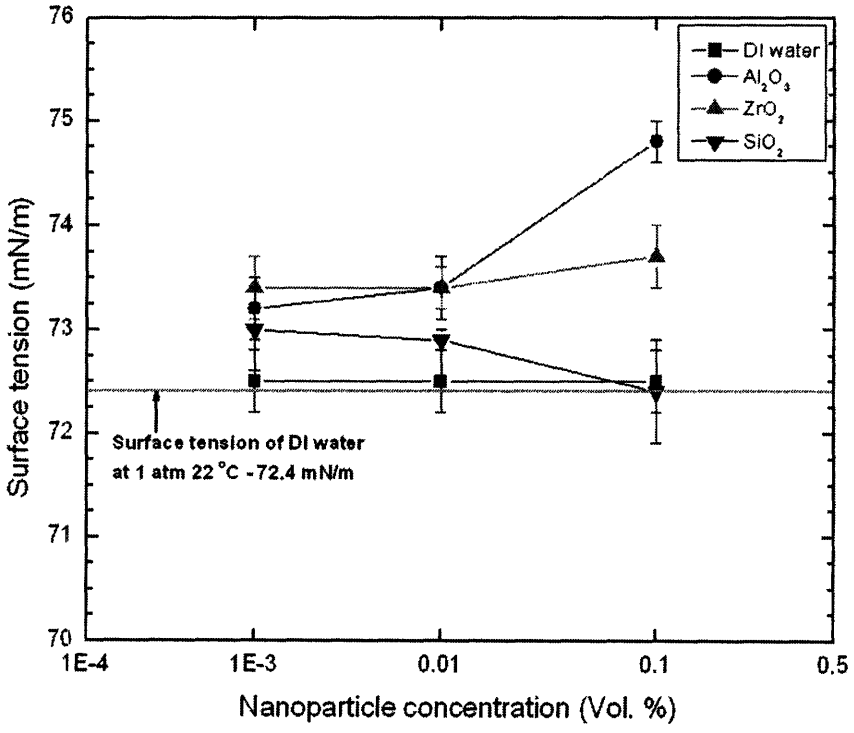


Figure 2-3 Variation of surface tension of tested nanofluids

## 2.5 THERMAL CONDUCTIVITY MEASURMENT

The thermal conductivity of nanofluids was measured with a KD2 handheld meter, a schematic diagram of which is given in Fig. 2-4. The range of the measurement is from 0.02 to 2.00 W/m·K with an accuracy of 0.01 W/m·K, or about 5% at full range. The operating temperature is from -20 to 60 °C. The KD2 probe uses the single-needle heat pulse technique to measure the thermal conductivity and thermal diffusivity of solid and fluid media. With this technique, a 30-second heat pulse is applied to the needle, and the temperature response with time is monitored. The temperature vs time response depends on the thermal properties of the material. To facilitate the understanding of the measurement, the theory is explained next.

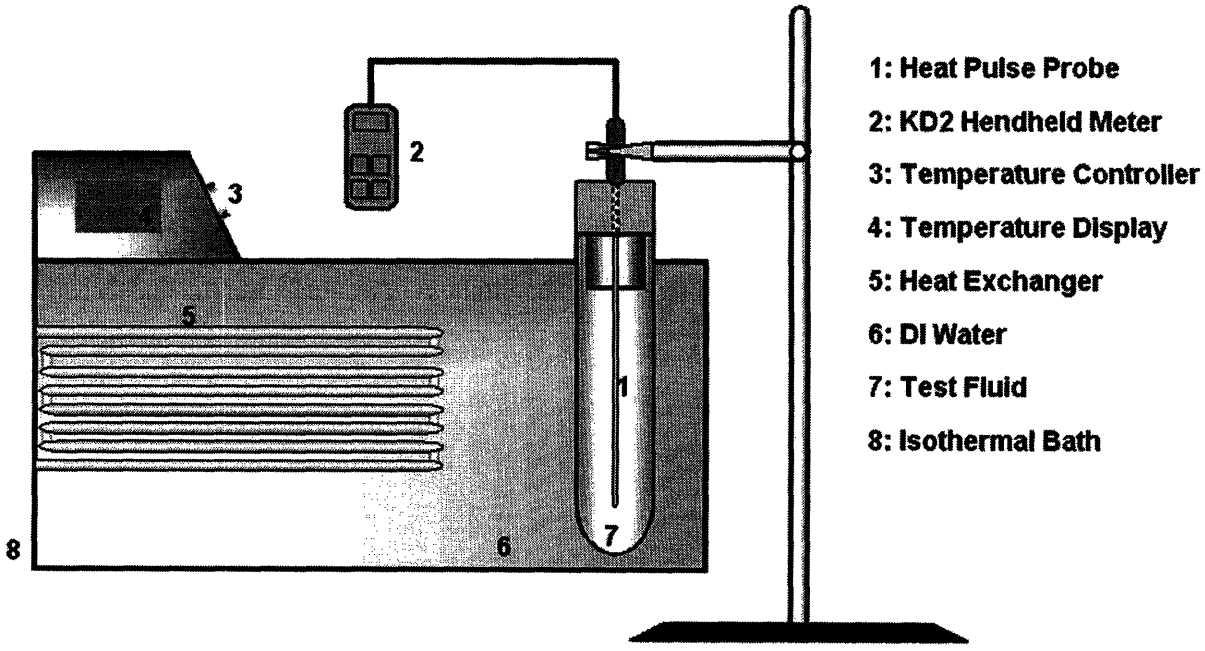


Figure 2-4 A schematic of thermal conductivity measurement

First the transient heat conduction equation for cylindrical coordinate in a homogeneous and isotropic medium is considered as the governing equation:

$$\frac{\partial T}{\partial t} = \alpha\left(\frac{\partial^2 T}{\partial r^2} + \frac{1}{r}\frac{\partial T}{\partial r}\right) \tag{2-5}$$

Where $T$ is temperature (°C), $t$ is time (second), $\alpha$ is thermal diffusivity ($m^2/s$), and $r$ is the radial distance (m) from the axis of the probe. Eq. (2-5) assumes negligible axial conduction and no convection effects. When a long, electrically heated probe is inserted into a medium, the temperature rise from an initial temperature, $T_i$, at some radial distance from the probe is

$$T - T_i = \left(\frac{q'}{4\pi k_h}\right) Ei\left(-\frac{r^2}{4\alpha t}\right) \tag{2-6}$$

Where $q'$ is the heat rate supplied per unit length (W/m) and $Ei$ is the exponential integral function given by

$$-Ei(-a) = \int_a^\infty \left(\frac{1}{u}\right)\exp(-u)du = -\gamma - \ln\left(\frac{r^2}{4\alpha t}\right) + \frac{r^2}{4\alpha t} - \left(\frac{r^2}{8\alpha t}\right) + \ldots \tag{2-7}$$

Where $a=r^2/4\alpha t$ and $\gamma$ is Euler's constant (0.5772). When $t$ is large, the higher order terms can be ignored, thus combining Eqs. (2-6) and (2-7) yields

$$\Delta T = T - T_i \cong \frac{q'}{4\pi k_h}\left[\ln t - \gamma - \ln\left(\frac{r^2}{4\alpha t}\right)\right] \tag{2-8}$$

Where $k_h$ is the thermal conductivity of the medium (W/m·K).

It is apparent from the relationship between thermal conductivity and $\Delta T=T-T_i$, shown in Eq. (2-8), that $\Delta T$ and $\ln(t)$ are linearly related with a slope $m=q'/4\pi k_h$. Linearly regressing $\Delta T$ on $\ln(t)$ yields a slope that, after arranging, gives the thermal conductivity as

$$k_h = \frac{q'}{4\pi m} \tag{2-9}$$

Where $q'$ is known from power supplied to the probe. The diffusivity can also be obtained from Eq. (2-8). The intersection of regression line with the $t$ axis ($\Delta T=0$) gives

$$\ln(t_o) = \left[\gamma + \ln\left(\frac{r^2}{4\alpha}\right)\right] \tag{2-10}$$

From the calculated $t_o$ (from the intercept of $\Delta T$ vs. $\ln(t)$) and finite $r$, Eq. (2-10) gives diffusivity, $\alpha$.

Because the higher order terms of Eq. (2-7) have been neglected, Eq. (2-8) is not exact. However, if the slope of intercept are computed only for $\Delta T$ and $\ln(t)$ values, where $t$ is large enough to ignore the higher order terms, Eqs. (2-9) and (2-10) give correct values for $k_h$ and $\alpha$.

From a physical view point, thermal conductivity of a material is a measure of how well the material conducts heat from one point to another in response to a temperature difference between two points. Conduction is defined as the heat transfer by means of molecular agitation within a material without any motion of the bulk material. Therefore it is important to eliminate any free convective heat transfer condition during the entire measurement. This is done by eliminating large thermal gradients within the system. That is, the test fluid sample is maintained at constant temperature by an isothermal bath, and the duration of the heat pulse in the probe is kept relatively short (a few seconds).

Thermal conductivity was measured at 0.1 MPa and 22.3°C using an isothermal bath. The results are given in Table 5. The thermal conductivity of dilute nanofluids does not show significant change compared to that of water. The measurement error is estimated to be about 2.2 %. The measured values for water are in good agreement with the value in NIST database (0.6025 W/m·K) for water at 0.1 MPa and 22.3 °C.

Table 5 Thermal conductivity of DI water and nanofluids measured with KD2

| | Nanoparticle concentration (v%) | Test 1 | Test 2 | Test 3 | Test 4 | Test 5 | **Average** |
|---|---|---|---|---|---|---|---|
| DI Water | 0 | 0.58 | 0.59 | 0.57 | 0.59 | 0.60 | 0.59 |
| $Al_2O_3$ | 0.1 | 0.58 | 0.59 | 0.57 | 0.60 | 0.59 | 0.59 |
| | 0.01 | 0.57 | 0.59 | 0.59 | 0.60 | 0.59 | 0.59 |
| | 0.001 | 0.57 | 0.59 | 0.59 | 0.59 | 0.55 | 0.58 |
| $ZrO_2$ | 0.1 | 0.60 | 0.60 | 0.59 | 0.58 | 0.59 | 0.59 |
| | 0.01 | 0.60 | 0.59 | 0.59 | 0.59 | 0.59 | 0.59 |
| | 0.001 | 0.58 | 0.58 | 0.59 | 0.59 | 0.59 | 0.59 |
| $SiO_2$ | 0.1 | 0.59 | 0.59 | 0.59 | 0.59 | 0.59 | 0.59 |
| | 0.01 | 0.58 | 0.58 | 0.59 | 0.59 | 0.59 | 0.59 |
| | 0.001 | 0.58 | 0.59 | 0.57 | 0.59 | 0.61 | 0.59 |

## 2.6 KINEMATIC VISCOSITY MEASUREMENT

A reverse-flow type Cannon-Fenske capillary viscometer for both opaque and transparent liquids was used to measure the kinematic viscosity of DI water as well as nanofluids. The measurable range is from $8\times10^{-7}$ to $4\times10^{-6}$ $m^2$/sec. The viscosity of pure water is $9.566\times10^{-7}$ $m^2$/sec at 22 °C according to the NIST database. The uncertainty of the measurement, 0.16% was provided with 95% confidence of the calibration measurements relative to the primary standard, water at 20 °C and 1 atm. The viscosity measurement of all tested fluids was conducted at 22 °C and atmospheric pressure. Since the viscosity has a high dependence on temperature, the viscometer was housed in a plastic cylinder filled with an air, effectively constituting an isothermal vessel. The viscometer is shown in Fig. 2-5. The measurement consists of the following steps:

1) Clean the viscometer using suitable solvents, and dry by passing clean, dry filtered air through the instrument to remove the final traces of solvents. Periodically, traces of organic deposits should be removed with chromic acid or non-chromium cleaning solution.
2) Charge the sample into the viscometer, invert the instrument and apply suction to tube arm F, immersing tube E in the liquid sample, and draw liquid to mark G. Wipe clean arm E, and turn the instrument to its normal vertical position.
3) Place the viscometer into the holder, and insert it into the constant temperature bath. Align the viscometer vertically in the bath by means of a small plumb bob in tube F, if a

self-aligning holder has not been used.

4) Allow sample to flow through capillary tube H and approximately half-fill bulb B, stopping the meniscus in bulb B by placing a rubber stopper in tube E.
5) Allow approximately 10 minutes for the sample to come to bath temperature at 40 °C and 15 minutes at 100 °C. Make sure the meniscus in bulb B does not reach line K.
6) Remove the rubber stopper and allow the meniscus to travel upwards into bulbs C and D, using two clocks to measure the efflux times for the meniscus to pass from mark K to mark J, and from mark J to mark I.
7) Calculate the kinematic viscosity of the sample by multiplying the efflux time in seconds for each bulb by the viscometer constant for each bulb.
8) Repeat the measurement by evacuating the sample and start over the steps (1) to (7).

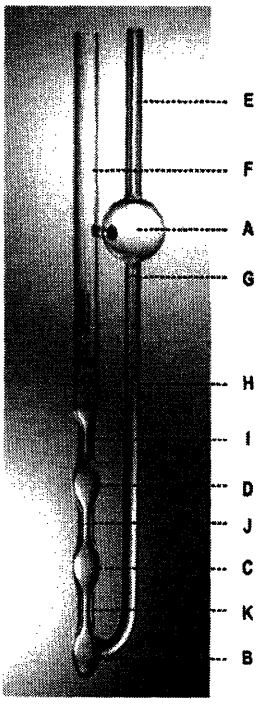


Figure 2-5 Cannon-Fenske capillary viscometer

The kinematic viscosity of DI water and nanofluids measured is tabulated in Table 6. In addition, its plots are given in Fig. 2-6. The results show that the viscosity of diluted nanofluids is not significantly different from that of DI water. The maximum fractional increases were observed for volumetric concentrations of 0.1% alumina, 0.01% zirconia, and 0.1% silica nanofluids, and were up to 2.2%, 1.0%, and 0.83%, respectively. This result reinforces the idea that transport properties do not change significantly in low concentrations of nanofluids.

Table 6 Kinematic viscosity of DI water and nanofluids measured at 22 °C and 1 atm

| Fluid | Nanoparticle concentration (v%) | Viscosity ($m^2$/sec) test 1 ($\times 10^7$) | Viscosity ($m^2$/sec) test 2 ($\times 10^7$) | **Average viscosity** ($m^2$/sec) ($\times 10^7$) |
|---|---|---|---|---|
| DI water | 0 | 9.28144 | 9.21552 | 9.24848 |
| $Al_2O_3$ | 0.001 | 9.30354 | 9.23174 | 9.26764 |
| | 0.01 | 9.32564 | 9.24797 | 9.28680 |
| | 0.1 | 9.45823 | 9.44266 | 9.45044 |
| $ZrO_2$ | 0.001 | 9.28144 | 9.37776 | 9.32960 |
| | 0.01 | 9.36983 | 9.31286 | 9.34135 |
| | 0.1 | 9.28144 | 9.31286 | 9.29715 |
| $SiO_2$ | 0.001 | 9.28144 | 9.18307 | 9.23225 |
| | 0.01 | 9.32564 | 9.19929 | 9.26246 |
| | 0.1 | 9.36983 | 9.28041 | 9.32512 |

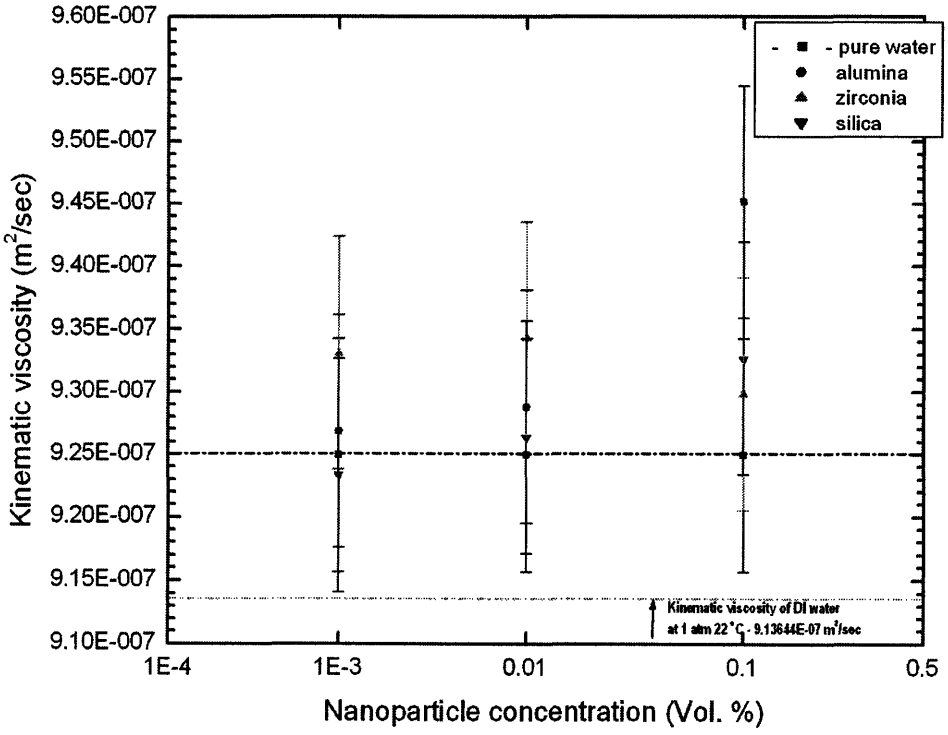


Figure 2-6 Kinematic viscosity of pure water and nanofluids

## 2.7 NANOPARTICLE SIZE MEASUREMENT

Nanoparticle size distribution in nanofluids is measured using Dynamic light scattering (DLS). DLS is a well established technique for measuring particle size over the range from a few nanometers to a few microns. The concept uses the idea that small particles in a suspension move in a random pattern. A microbiologist by the name of Brown first discovered this effect while observing objects thought to be living organisms, by light microscopy. Later it was determined that the "organisms" were actually particles, but the term has endured. Thus, the movement of small particles in a resting fluid is termed "Brownian Motion" and can easily be observed for particles of approximately 0.5 to 1.0 microns with a microscope at a magnification of 200 to 400X [35,36]. Observation of larger particles compared to smaller particles will show that the larger particles move more slowly than the smaller ones given the same temperature. According to Einstein's developments in his Kinetic Molecular Theory, molecules that are much smaller than the particles can impart a change to the direction of the particle and its velocity. Thus water molecules (0.00033 microns) can move polystyrene particles as large as a couple of microns. The combination of these effects is observed as an overall random motion of the particle.

A detailed technical description will help to understand the DLS measurement better. When a coherent source of light such as a laser having a known frequency is directed at the moving particles, the light is scattered, but at a different frequency. The change in the frequency is quite similar to the change in frequency or pitch one hears when an ambulance with its wailing

siren approaches and finally passes. The shift is termed a Doppler shift or broadening, and the concept is the same for light when it interacts with small moving particles. For the purposes of particle measurement, the shift in light frequency is related to the size of the particles causing the shift. Due to their average velocity, smaller particles cause a greater shift in the light frequency than larger particles. Thus, the difference in the frequency of the scattered light among particles of different sizes is used to determine the sizes of the particles present.

The DLS equipment used for this study consists of mainly three components. A laser provided by Spectra-Physics emits a 514 nm wavelength of argon. A goniometer from Brookhaven preserves any scattering between the incident laser and present nano-size particle, which is placed onto a bath. Finally, a detector from Brookhaven detects a laser scattered in 90 degrees from the incident laser since the angle between the goniometer and detector is fixed as 90 degrees. This configuration is well reflected in the Fig. 2-7. It is of importance to clarify the physical situation upon this scattering measurement. Since the expected particle size will be smaller than the wavelength of the incident laser, this type of scattering can be categorized as the Rayleigh scattering, which is defined as the scattering of light, or other electromagnetic radiation, by particles much smaller than the wavelength of the light.

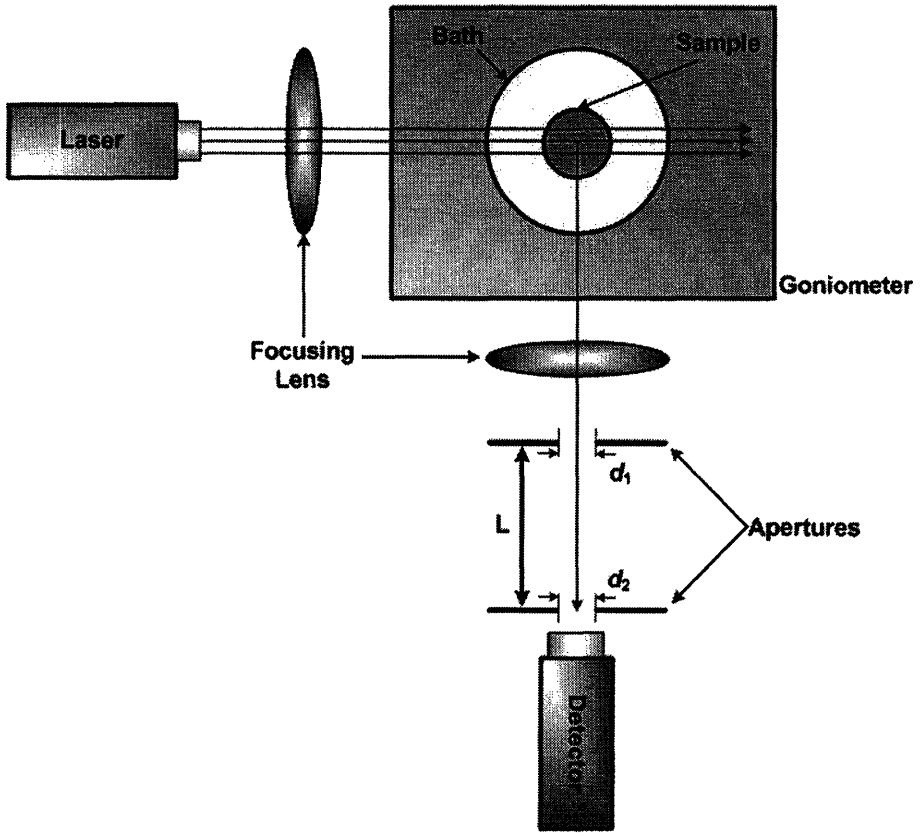


Figure 2-7 A schematic of light scattering measurement with a dynamic mode

In addition, an alternative mode of light scattering measurement, static light scattering, is also viable if the configuration allows the goniometer to rotate automatically. In such a case, scattered lasers will be detected according to the angle change, which gives the angular distribution of particle size. In either modes of dynamic or static, hydrodynamic or gyration particle sizes can be obtained, respectively.

When measuring a particle size, it is necessary to start with several assumptions. First the particles can be assumed to be in Brownian motion. Second, it assumed that the particle do not interact with each other. In a practical measurement, the second assumption can be valid

when the fluid contains a small number of particles. With those assumptions, the average motion of a particle can be described by using an intermediate scattering function, $f(q,\tau)$ expressed as:

$$f(q,\tau) = \langle \exp\{-iq \cdot [r(0) - r(\tau)]\} \rangle = \langle \exp[iq \cdot \Delta r(\tau)] \rangle \tag{2-11}$$

Where $q=(4\pi/\lambda)\sin(\theta/2)$ is a scattering factor, $\lambda$ is a wavelength of scattered light, $\theta$ is an angle between incident and scattered lights, $\tau$ is the time scale during the scattering, and $\Delta r(\tau) \equiv r(\tau) - r(0)$ is displacement of particle in time $\tau$.

For particle in Brownian motion, $\Delta r(\tau)$ is a real 3-D Gaussian variable and therefore $f(q, \tau)$ and the mean square displacement $\langle \Delta r^2(\tau) \rangle$ becomes:

$$f(q,\tau) = \exp\left[ -\frac{q^2}{6} \langle \Delta r^2(\tau) \rangle \right] \tag{2-12}$$

$$\langle \Delta r^2(\tau) \rangle = 6 D_o \tau \tag{2-13}$$

Combining Eqs. (2-12) and (2-13) yields:

$$f(q,\tau) = \exp\left[ -q^2 D_o \tau \right] \tag{2-14}$$

Where $D_o$ is a mass self-diffusion coefficient defined by Stokes-Einstein theory as:

$$D_o = \frac{k_B T}{6\pi\eta R} \tag{2-15}$$

Where $k_B$ is the Boltzmann constant, $T$ is the temperature, $\eta$ is viscosity, and $R$ is a radius of the particle that is measured.

In the measurement, the measured quantity indeed is the diffusion constant $D_o$ based on the known scaling factor $q$ and time $\tau$ in the Eq. (2-14). Using the obtained $f(q,\tau)$, the diffusion constant is found from Eq. (2-14). Finally, the radius of particle size $R$ is determined from Eq. (2-15),.

The results of the DLS particle size measurements are reported in Table 7 and the spectra are shown in Figs. 2-8 to 2-14. Interestingly, the particle size of silica dispersed in the DI water shows the similar number as described in the specification provided by the vendor, Applied Nanoworks. However, the particle sizes of alumina and zirconia dispersed in the water seem to be at least 5 times the particle size specified by the vendor. It is believed that particles suspended in the fluid can agglomerate and the process is exacerbated by changes in pH. This agglomeration effect becomes another subject of nanofluids research due to the fact that the nanofluid itself can lose its identity in terms of nature of "nano-scale".

Table 7 Particle size measured by DLS technique (n/a denotes that particle size detection was not viable because the nanofluids were diluted too much)

| | $Al_2O_3$ | | | $ZrO_2$ | | | $SiO_2$ | | |
|---|---|---|---|---|---|---|---|---|---|
| Nanoparticle concentration (v%) | 0.1 | 0.01 | 0.001 | 0.1 | 0.01 | 0.001 | 0.1 | 0.01 | 0.001 |
| Mean diameter (nm) | 132.6 | 133.6 | 113.7 | 136.5 | 496.1 | 226.6 | 21.5 | n/a | n/a |
| Effective diameter (nm) | 207.1 | 208.4 | 185.4 | 115.4 | 255.0 | 255.2 | 35.7 | n/a | n/a |

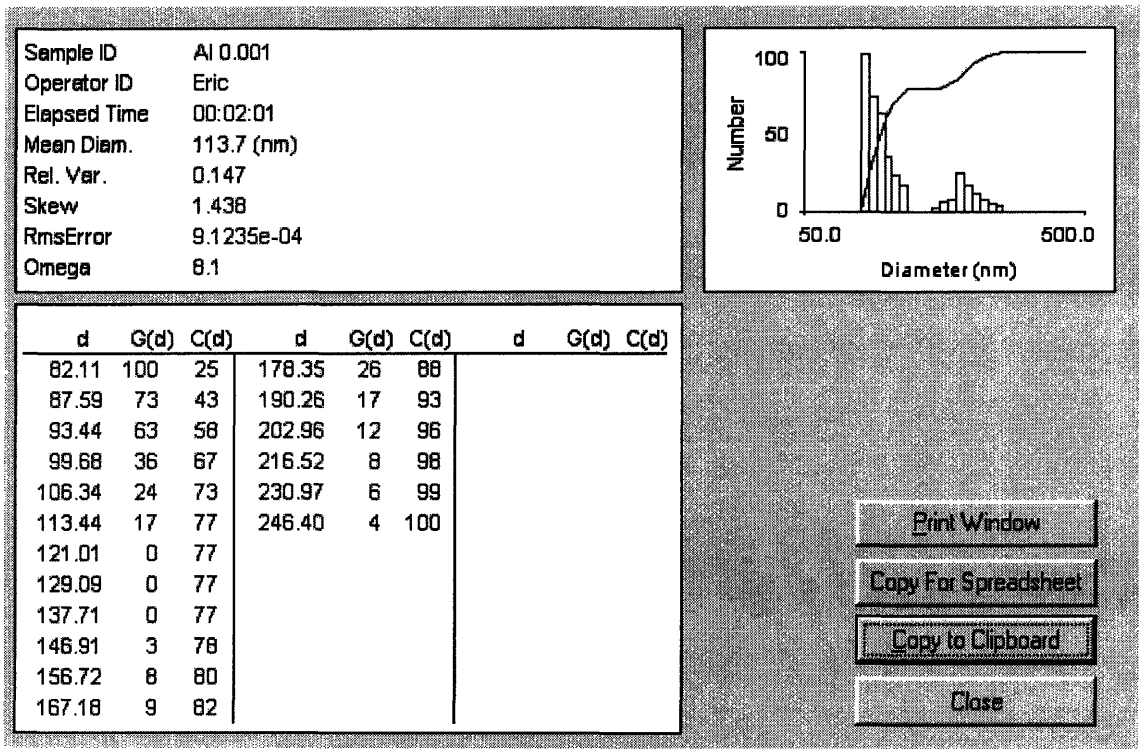


Figure 2-8 DLS measurement (0.001 v% $Al_2O_3$)

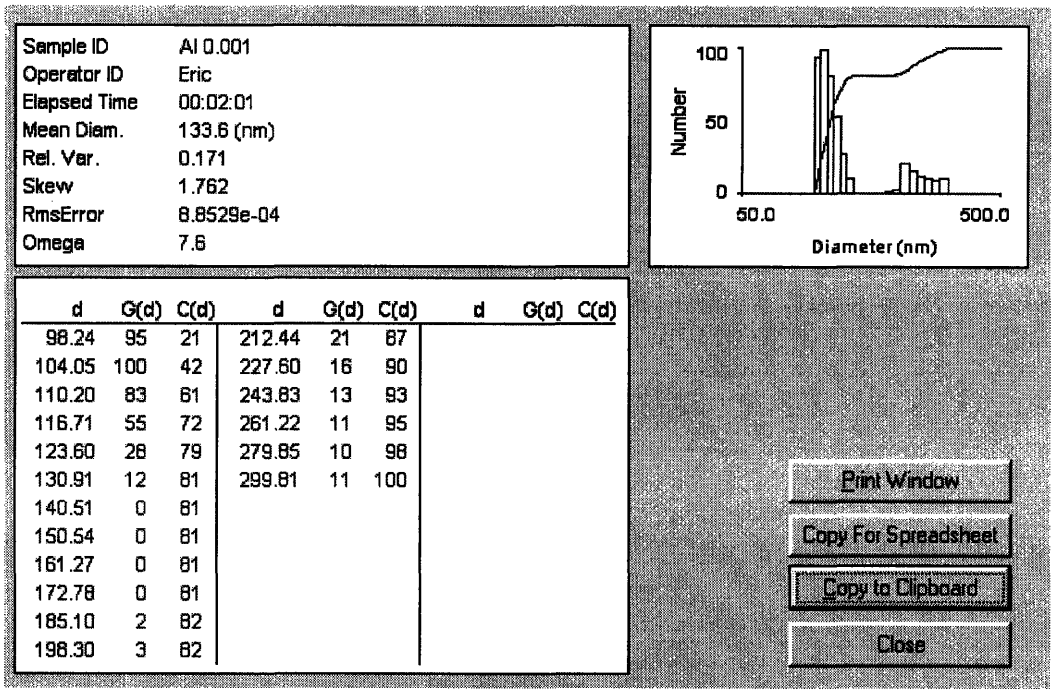


Figure 2-9 DLS measurement (0.01 v% $Al_2O_3$)

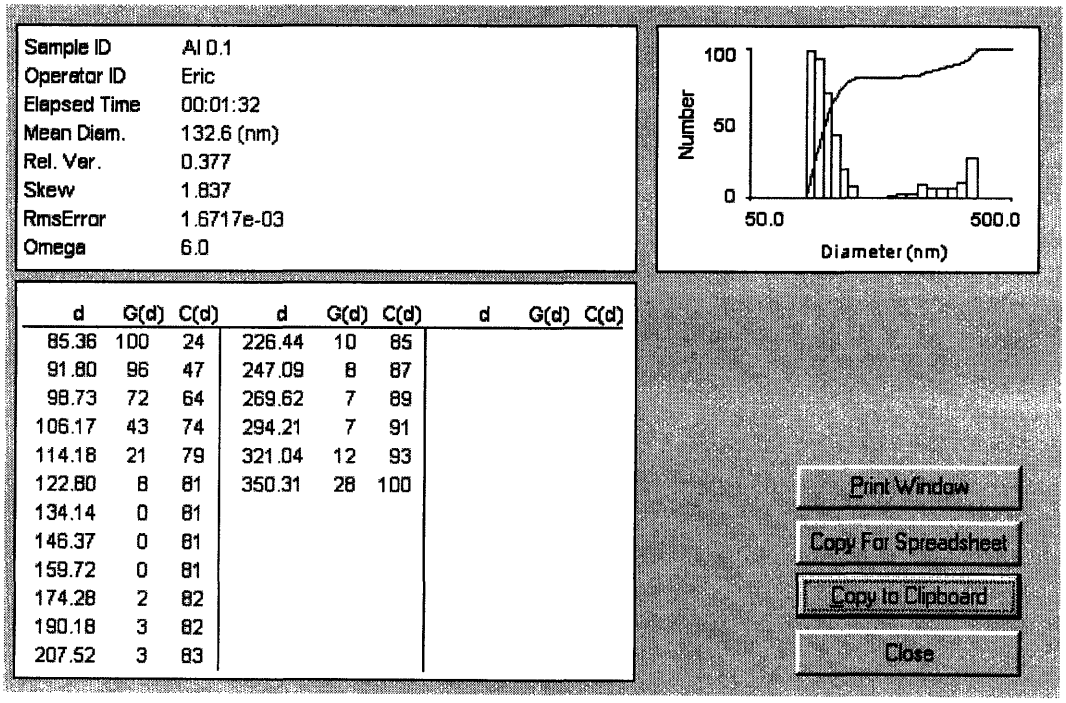


Figure 2-10 DLS measurement (0.1 v% $Al_2O_3$)

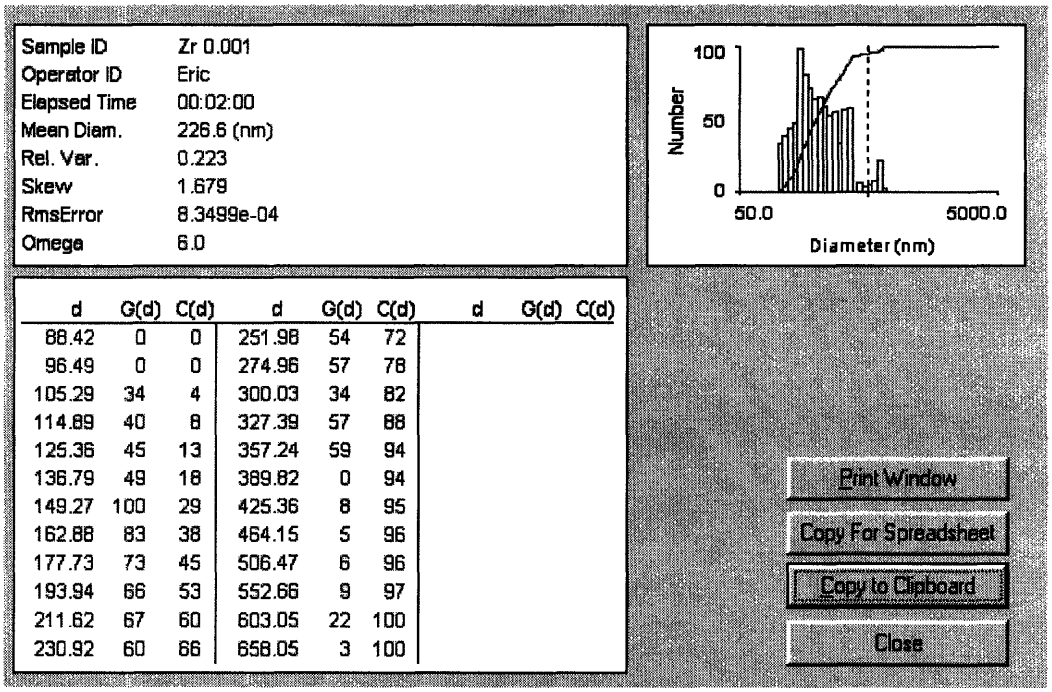


Figure 2-11 DLS measurement (0.001 v% $ZrO_2$)

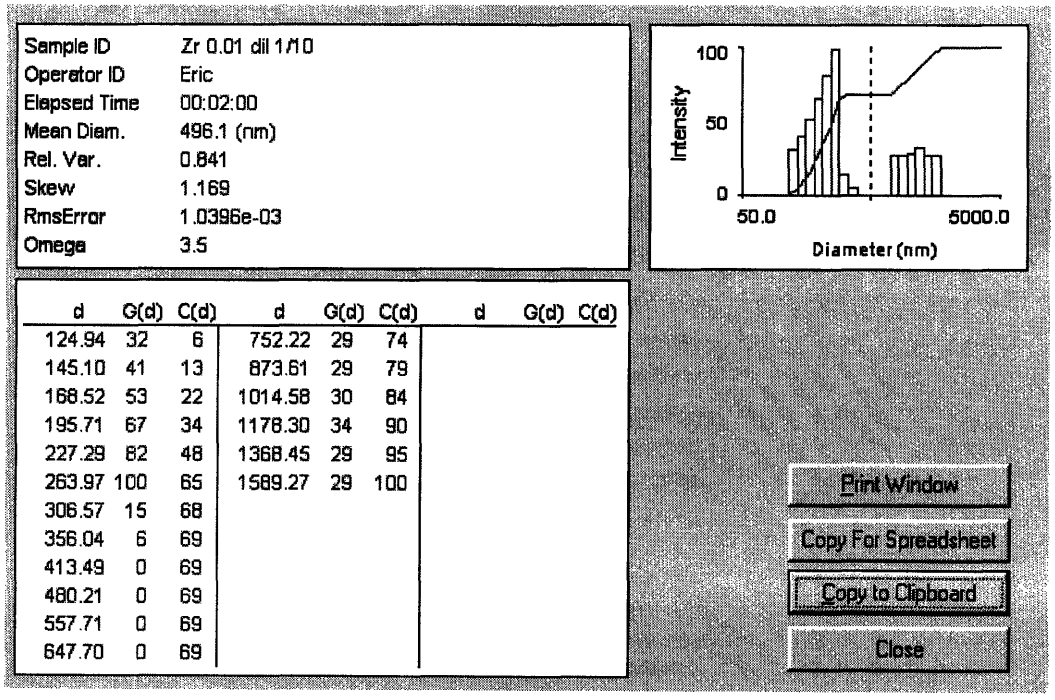


Figure 2-12 DLS measurement (0.01 v% $ZrO_2$)

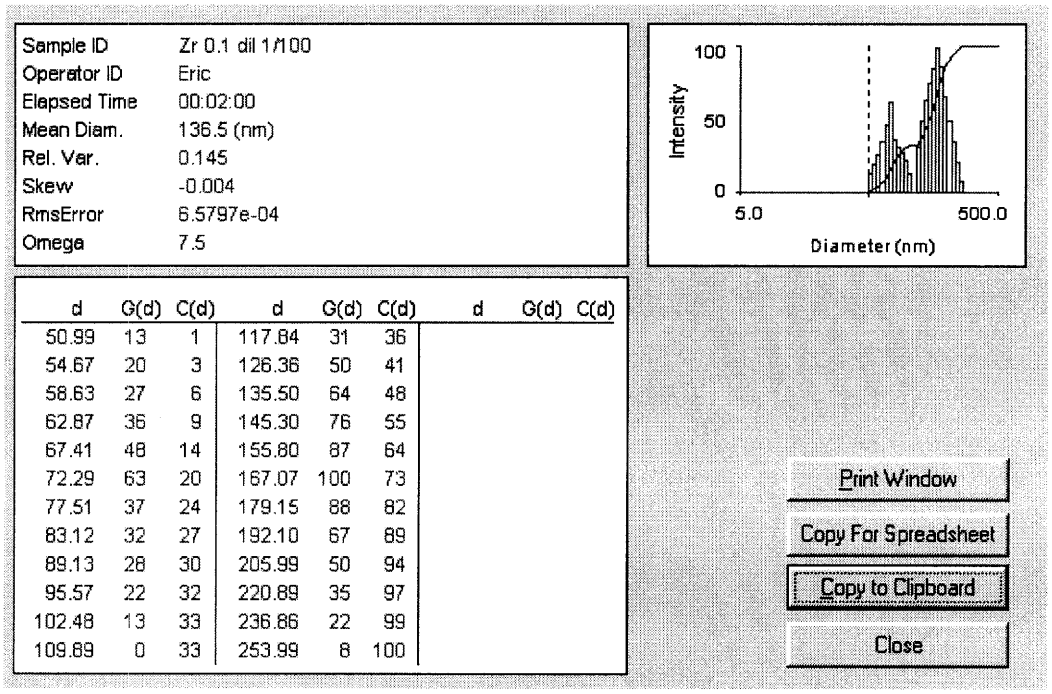


| d | G(d) | C(d) | d | G(d) | C(d) | d | G(d) | C(d) |
|---|---|---|---|---|---|---|---|---|
| 50.99 | 13 | 1 | 117.84 | 31 | 36 | | | |
| 54.67 | 20 | 3 | 126.36 | 50 | 41 | | | |
| 58.63 | 27 | 6 | 135.50 | 64 | 48 | | | |
| 62.87 | 36 | 9 | 145.30 | 76 | 55 | | | |
| 67.41 | 48 | 14 | 155.80 | 87 | 64 | | | |
| 72.29 | 63 | 20 | 167.07 | 100 | 73 | | | |
| 77.51 | 37 | 24 | 179.15 | 88 | 82 | | | |
| 83.12 | 32 | 27 | 192.10 | 67 | 89 | | | |
| 89.13 | 28 | 30 | 205.99 | 50 | 94 | | | |
| 95.57 | 22 | 32 | 220.89 | 35 | 97 | | | |
| 102.48 | 13 | 33 | 236.86 | 22 | 99 | | | |
| 109.89 | 0 | 33 | 253.99 | 8 | 100 | | | |

Figure 2-13 DLS measurement (0.1 v% $ZrO_2$)

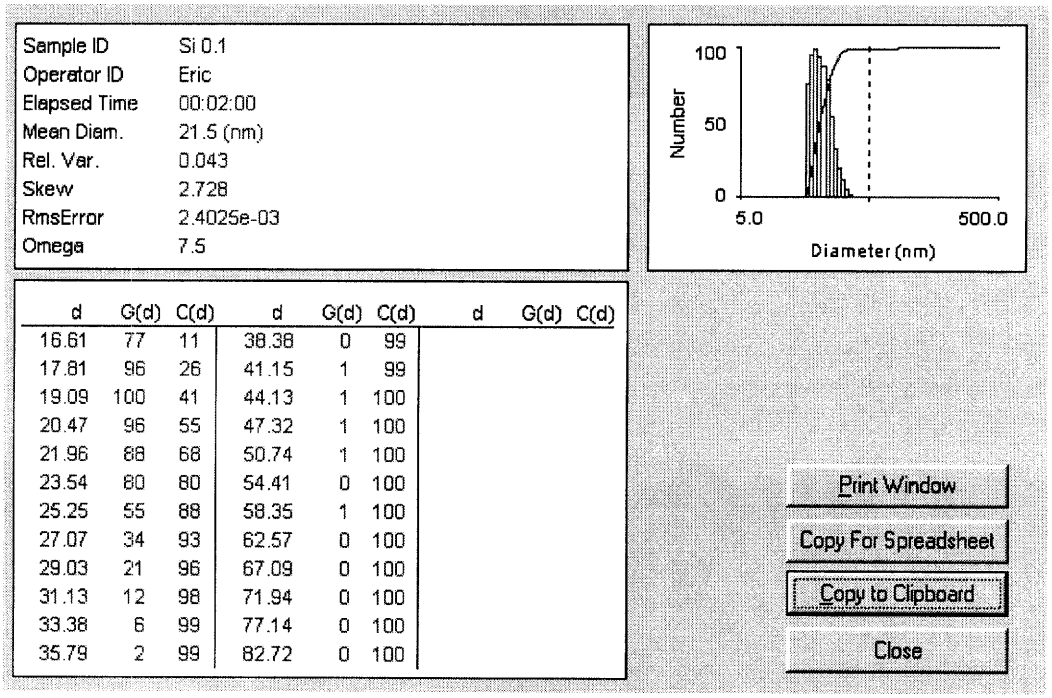


| d | G(d) | C(d) | d | G(d) | C(d) | d | G(d) | C(d) |
|---|---|---|---|---|---|---|---|---|
| 16.61 | 77 | 11 | 38.38 | 0 | 99 | | | |
| 17.81 | 96 | 26 | 41.15 | 1 | 99 | | | |
| 19.09 | 100 | 41 | 44.13 | 1 | 100 | | | |
| 20.47 | 96 | 55 | 47.32 | 1 | 100 | | | |
| 21.96 | 88 | 68 | 50.74 | 1 | 100 | | | |
| 23.54 | 80 | 80 | 54.41 | 0 | 100 | | | |
| 25.25 | 55 | 88 | 58.35 | 1 | 100 | | | |
| 27.07 | 34 | 93 | 62.57 | 0 | 100 | | | |
| 29.03 | 21 | 96 | 67.09 | 0 | 100 | | | |
| 31.13 | 12 | 98 | 71.94 | 0 | 100 | | | |
| 33.38 | 6 | 99 | 77.14 | 0 | 100 | | | |
| 35.79 | 2 | 99 | 82.72 | 0 | 100 | | | |

Figure 2-14 DLS measurement (0.1 v% $SiO_2$)

# 3 POOL BOILING WIRE AND FLAT HEATER EXPERIMENT

## 3.1 CHF EXPERIMENTS WITH WIRE

The CHF of deionized pure water and nanofluids was measured in the apparatus shown in Fig. 3-1, which consists of a wire heater horizontally submerged in the test fluid at atmospheric pressure, surrounded by an isothermal bath. The wire is made of stainless steel grade 316, has a 0.381-mm diameter and 12-cm length. The wire is soft soldered with a silver-lead solder to the copper electrodes and heated by resistance heating with a DC power supply of 20-V and 120-A capacity. Voltage and current are measured with Keithley and Hewlett-Packard multimeters. The wire temperature is estimated using an electrical resistance-temperature relation, $R=R_o[1+\alpha(T-T_o)]$, where the resistances $R$ and $R_o$ are measured as the current increases and at the saturation temperature of water before the wire heater is heated up, respectively. The reference temperature, $T_o$ is assumed to be the saturation temperature of water at atmospheric pressure. Therefore, with the known average temperature coefficient of resistivity, $\alpha$ of 0.0006, the wire temperature $T$ can be obtained. It should be noted that the temperature coefficient of resistivity, $\alpha$, is known to have a relatively large uncertainty in its value because the wire heater is made of stainless steel grade 316, which is an alloy of various materials of iron, chromium, nickel, molybdenum, and carbon etc. The fluid bulk temperature is measured with a K-type thermocouple (nominal uncertainty ±1.1°C, as specified by the manufacturer).

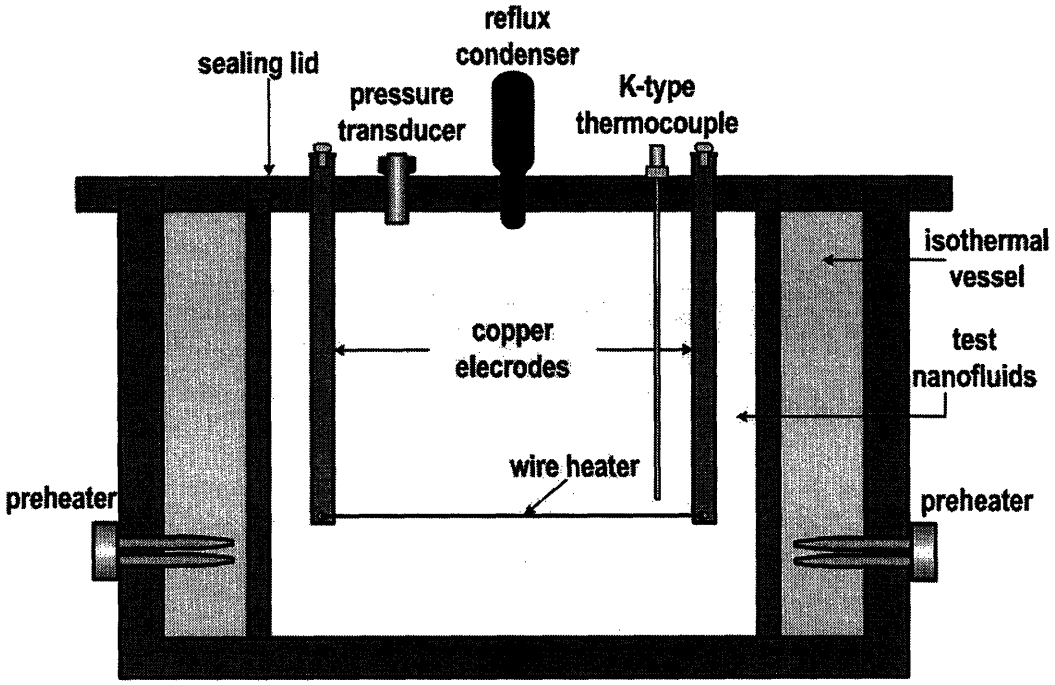


Figure 3-1 A schematic of resistance heating wire pool boiling facility

The experimental procedure is as follows. First, the isothermal bath and the test fluids are taken to the desired temperature by the preheaters. The wire is heated up at low heat flux to remove any noncondensable gas bubbles sticking to the surface. After the gas is removed, the power is increased in small steps of ~0.2 V until CHF occurs. CHF is detected visually (i.e., the wire glows) and/or electrically (i.e., the electric resistance suddenly increases), thus terminating the experiment. Heat fluxes are calculated from the following equation:

$$q'' = \frac{IV}{\pi LD} \tag{3-1}$$

The uncertainties on the current, voltage, heated length and wire diameter values are less than 3%, 4%, 3% and 1%, respectively, resulting in an uncertainty of less than 6% on the heat flux. Measured CHF values are shown in Fig. 3-2. Significant CHF enhancement is observed for all nanofluids, up to 52% with alumina nanofluids, up to 75% with zirconia nanofluids and up to 80% for silica nanofluids. The CHF dependence on nanoparticle concentration is a bit erratic, but not unprecedented for nanofluids [10].

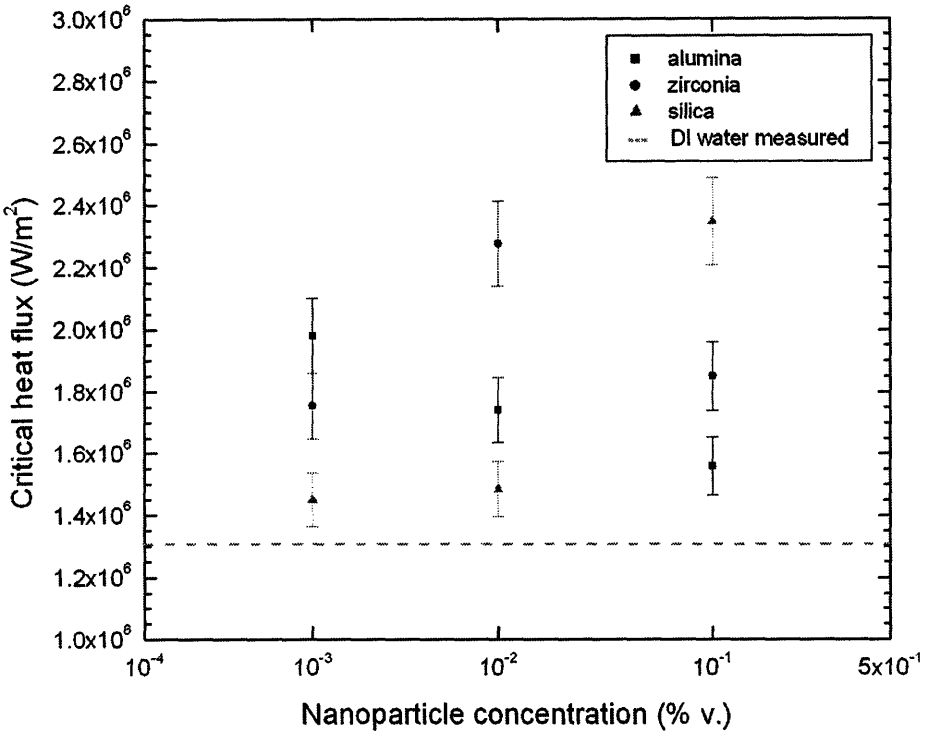


Figure 3-2 CHF data for DI water and alumina, zirconia and silica nanofluids

The boiling regimes of pure water and a nanofluid are compared in Fig. 3-3. At the low heat flux (Fig. 3-3a and 3-3b), both fluids are in the nucleate boiling regime. At the high heat flux, pure water has exceeded CHF and thus a stable vapor film blankets the wire (film boiling), which is glowing red (Fig. 3-3c). However, the nanofluid (Fig. 3-3d) is still well within the nucleate boiling regime.

(a) Pure water (0.5 MW/m$^2$)

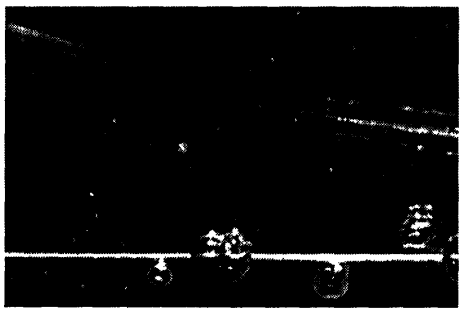

(b) Nanofluid (0.5 MW/m$^2$)

(c) Pure water (1 MW/m$^2$)

(d) Nanofluid (1 MW/m$^2$)

Figure 3-3 Pool boiling of pure water and 0.01 v% alumina nanofluid at the same heat flux on the wire heater

Typical boiling curves for pure water and three nanofluids are shown in Fig. 3-4. Note that the nanofluids have higher CHF, but lower nucleate boiling heat transfer coefficient. The

deterioration of nucleate boiling suggests that a surface effect may be at work. This result is consistent with the experimental results reported in ref. [5,10,5]. Controversially, however, some studies report enhancement of heat transfer coefficient [7,12,16].

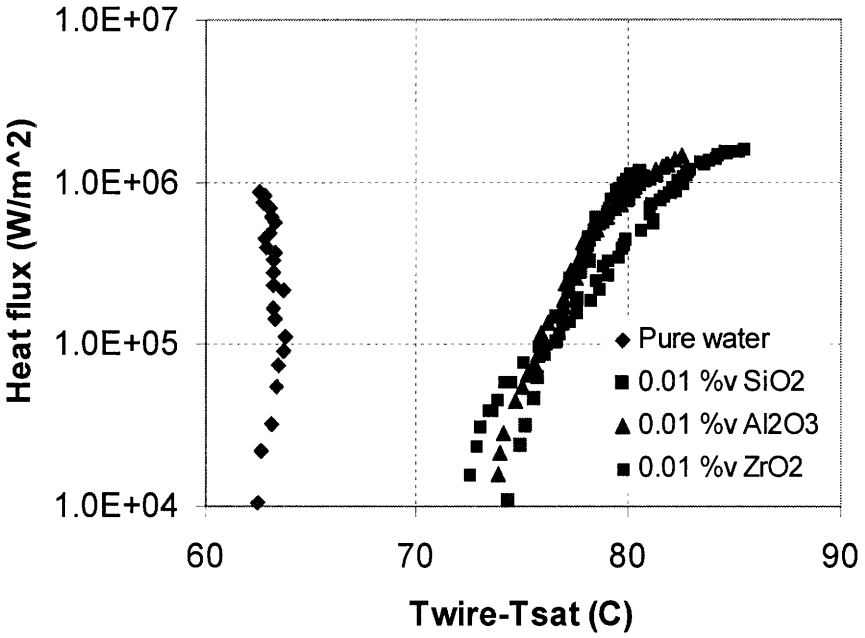


Figure 3-4 Boiling curves for wire heater[1]

Scanning Electron Microscopy (SEM) analysis of the wire surface reveals that the surface is clean during pure water boiling (Fig. 3-5a), but a porous layer builds up during nanofluid boiling (Fig. 3-5b). It is believed that this layer is due to nanoparticle precipitation caused by nucleate boiling. EDS analysis of the layer confirms that it is made of nanoparticle material. The presence of a porous layer on the surface undoubtedly has an impact on boiling heat

[1] Uncertainties in the slope of the resistivity-temperature curve for stainless steel and the non-negligible temperature drop within the wire contribute to the unusually high values of the superheat in this boiling curve.

transfer through changes in surface area, roughness, and wettability, as explained in the following sections.

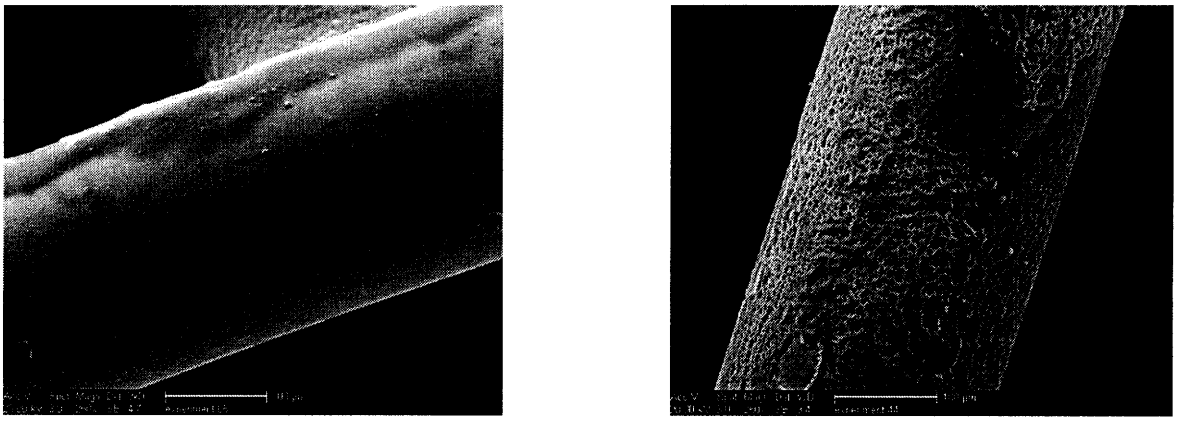

(a) Pure water (b) Nanofluid

Figure 3-5 SEM images of wire heaters taken after boiling pure water and 0.01 v% alumina nanofluid

## 3.2 WETTABILITY EXPERIMENTS WITH FLAT HEATER

### 3.2.1 Experimental Apparatus

Use of a thin wire heater is convenient for CHF experiments, but its high curvature makes it inconvenient for surface analysis, such as required to study the porous layer. For this purpose, flat plates of 5 mm wide, 45 mm long, 0.05 mm thick, made of stainless steel grade 316 were introduced, whose schematics are given in Fig. 3-6. Using the apparatus of Figs. (3-1) and (3-6b), several flat heaters were boiled in nanofluids for a period of 5 minutes and at a heat flux of 500 kW/m$^2$. A new (clean) heater was used for each experimental run.

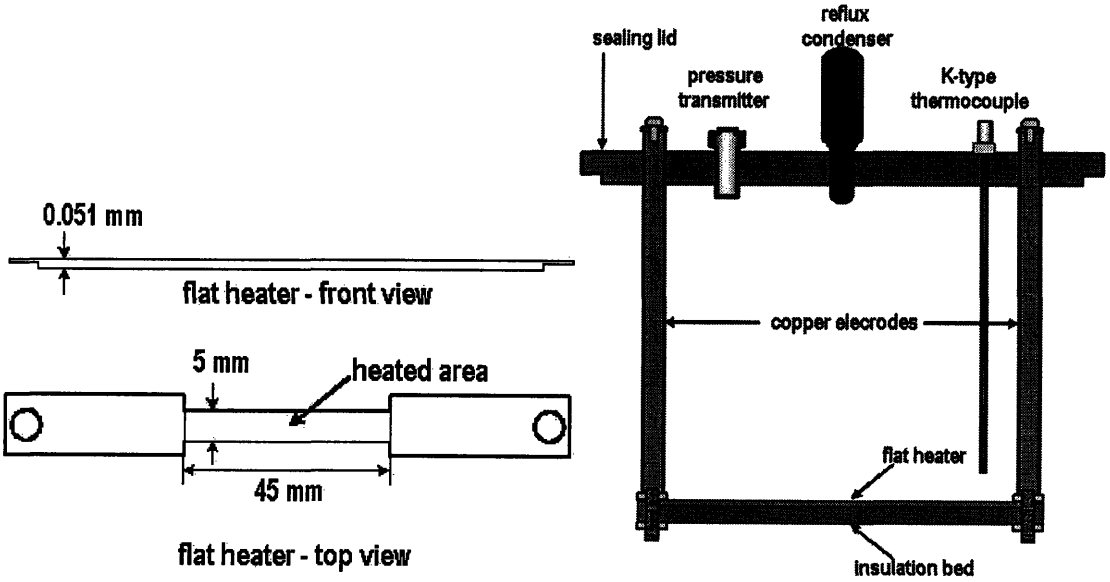


(a) (b)

Figure 3-6 Schematics of (a) flat heater and (b) heater assembly

Another significant investigation consistent with the primary goal of the current study is to measure the contact angle to confirm any improvement in wettability of the fouled surfaces. The degree of wettability is traditionally related to the contact angle. As the contact angle becomes lower, it is expected that better surface wettability can be obtained. An increase in surface wettability can be an important factor in explaining the remarkable enhancement of CHF with nanofluids.

In order to find such a clue, wetting experiments using a sessile drop technique were performed in which pictures of the contact angle are taken and its numeric value is estimated. A state-of-the-art contact angle goniometer, EasyDrop Contact Angle Instrument by Krüss, was used with a resolution of 0.1 degree in the measuring range of 1 to 180 degree. The picture of the apparatus is given in Fig. 3-7. A monochrome interline CCD camera with 25/30 fps helps to obtain accurate results when the drop is fitted automatically. Fitting the angle, width-height associated with contour fitting is used to get a numeric value of the contact angle. It is recommended to use a consistent volume of sessile drop during each test. The volume was kept below 5 μl throughout the entire tests. Also, the time duration of the measurement was kept short enough less than 30 seconds to minimize droplet evaporation. The measurement was carried out at 22 $^{o}$C in air by depositing each nanofluid drop on a surface fouled with the same nanofluid. For example, a drop of 0.1 v% of $Al_2O_3$ nanofluid was deposited on the fouled surface boiled in the 0.1 v% of $Al_2O_3$ nanofluid.

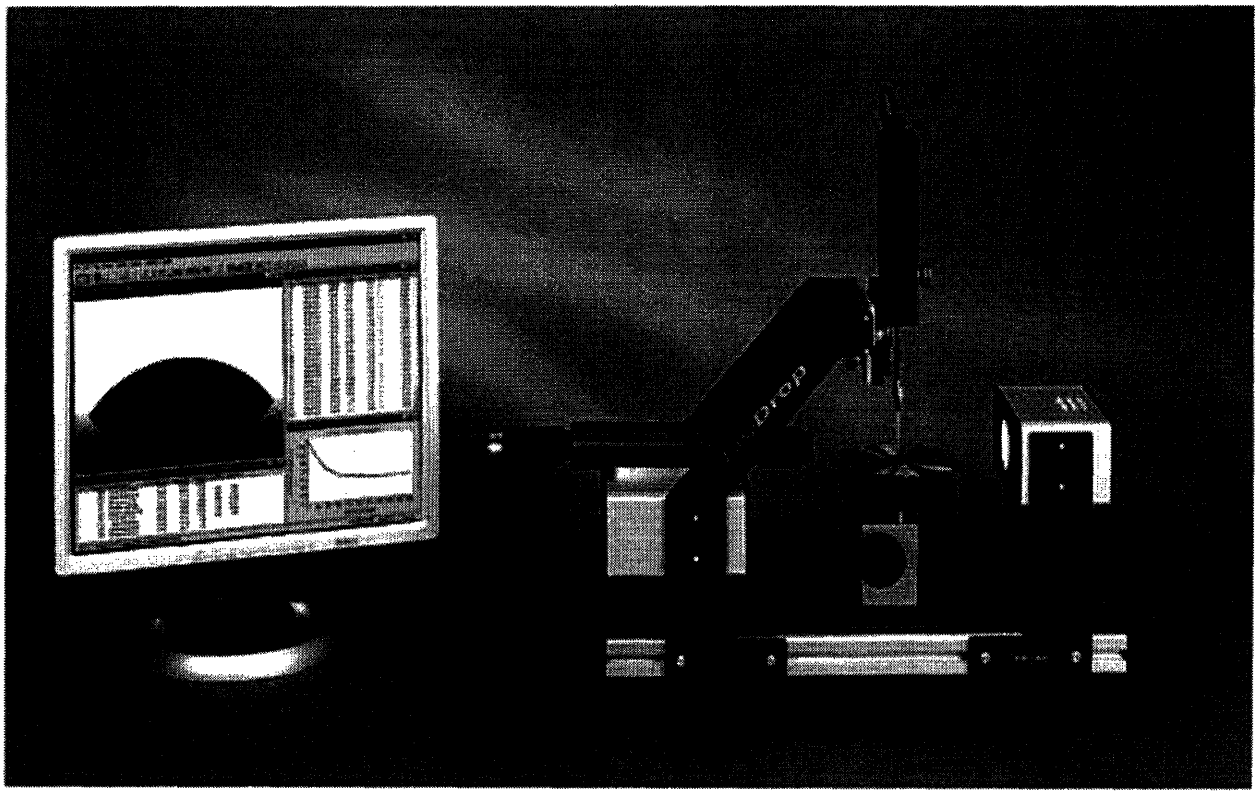

Figure 3-7 Contact angle measurement (EasyDrop Contact Angle Instrumentation by Krüss)

### 3.2.2 Contact Angle Measurement

The static contact angle, θ, was measured for sessile droplets of DI water and nanofluids at 22°C in air on the clean and nanoparticle-fouled surfaces boiled in nanofluids. A typical schematic of the static contact of liquid in the vapor/solid interface is given in Fig. 3-8. The uncertainty on such measurements is estimated to be ±10°. Low values of the contact angle correspond to high surface wettability.

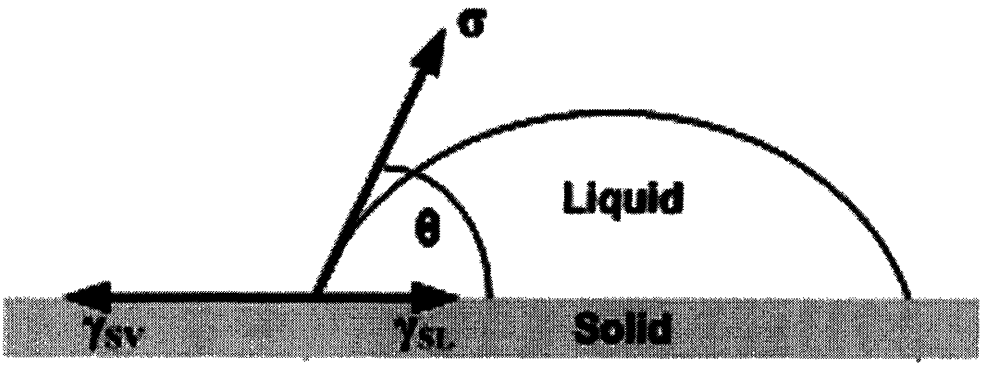


Figure 3-8 A schematic of static contact angle of liquid

Several representative cases are shown in Figs. 3-9 through 18. In addition, the complete contact angle database is reported in Table 8. A rather dramatic decrease of the contact angle on the fouled surfaces is evident. Such decrease occurs with DI water as well as nanofluid droplets, and thus suggests that wettability is enhanced by the porous layer on the surface, not the nanoparticles in the fluid. In another research, Wasan and Nikolov [19] found that ordering of nanoparticles near the liquid/solid contact line can improve the spreading of

nanofluids.

Table 8 Static contact angles for DI water and nanofluids on clean and fouled surfaces

| Fluid | DI water | $Al_2O_3$ nanofluid | | | $ZrO_2$ nanofluid | | | $SiO_2$ nanofluid | | |
|---|---|---|---|---|---|---|---|---|---|---|
| Nanoparticle concentration (v%) | 0 | 0.001 | 0.01 | 0.1 | 0.001 | 0.01 | 0.1 | 0.001 | 0.01 | 0.1 |
| Clean surface | 79° | 80° | 73° | 71° | 80° | 80° | 79° | 71° | 80° | 75° |
| Nanofluid boiled surface | 8°-36° [a] | 14° | 23° | 40° | 43° | 26° | 30° | 11° | 15° | 21° |

[a] 22°-30° on surfaces boiled in alumina nanofluids, 16°-36° on surfaces boiled in zirconia nanofluids, 8°-18° on surfaces boiled in silica nanofluids.

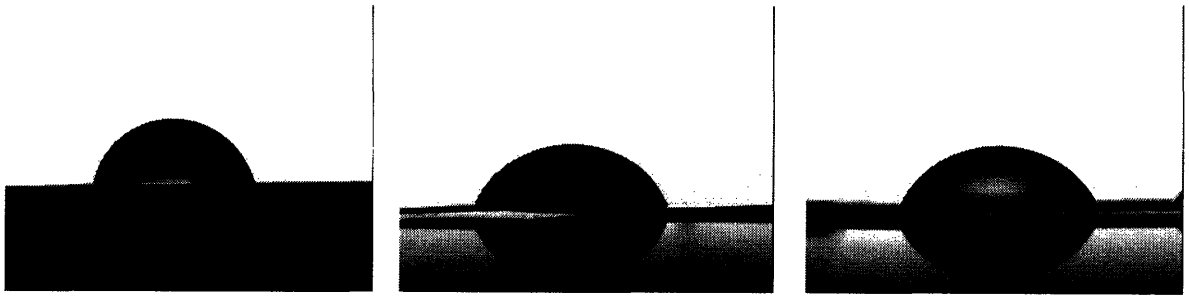

(a) 79° (b) 72° (c) 65.4°

Figure 3-9 Contact angle of (a) DI water and (b) 0.1 v% of $Al_2O_3$ on the flat heater boiled in the DI water; (c) 0.001 v% of $ZrO_2$ on the bare flat heater

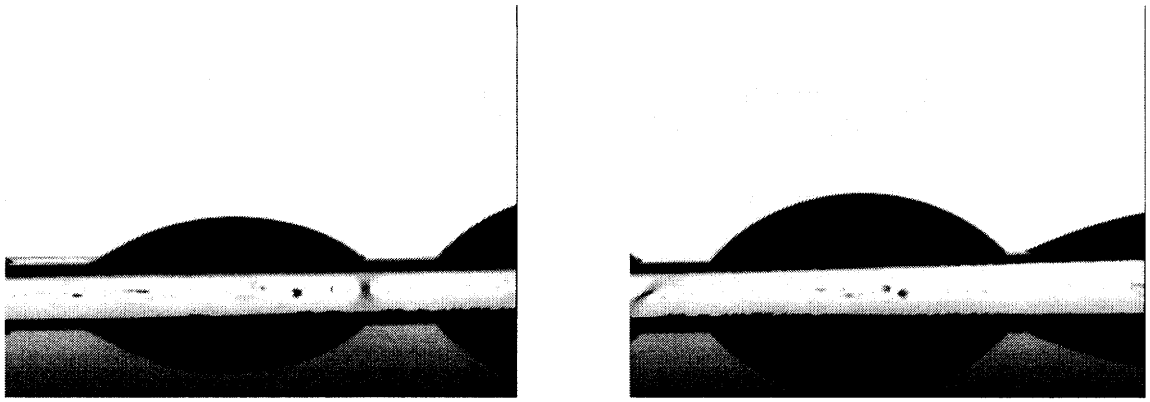

(a) 39.6° (b) 41.1°

Figure 3-10 Contact angle of 0.1v% of $Al_2O_3$ on the flat heater boiled in the 0.1 v % $Al_2O_3$

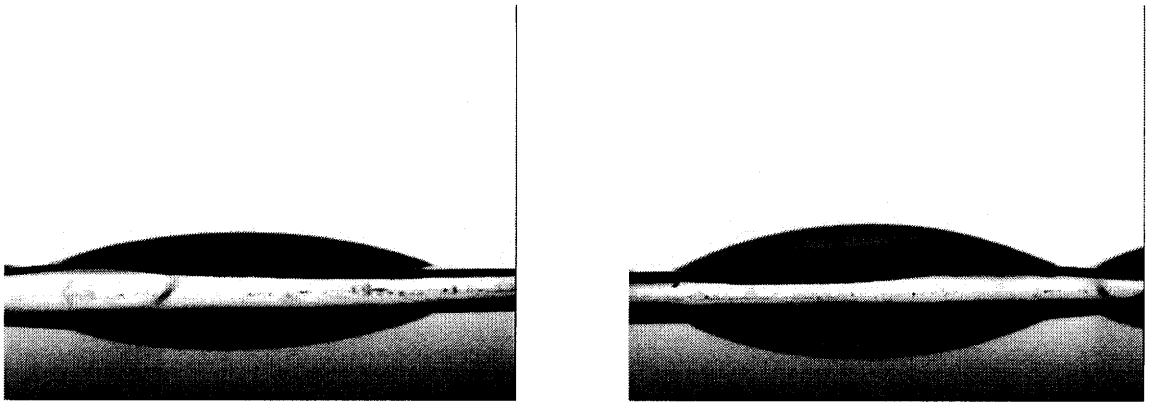

(a) 18° (b) 27.8°

Figure 3-11 Contact angle of 0.01 v% of $Al_2O_3$ on the flat heater boiled in the 0.01 v % $Al_2O_3$

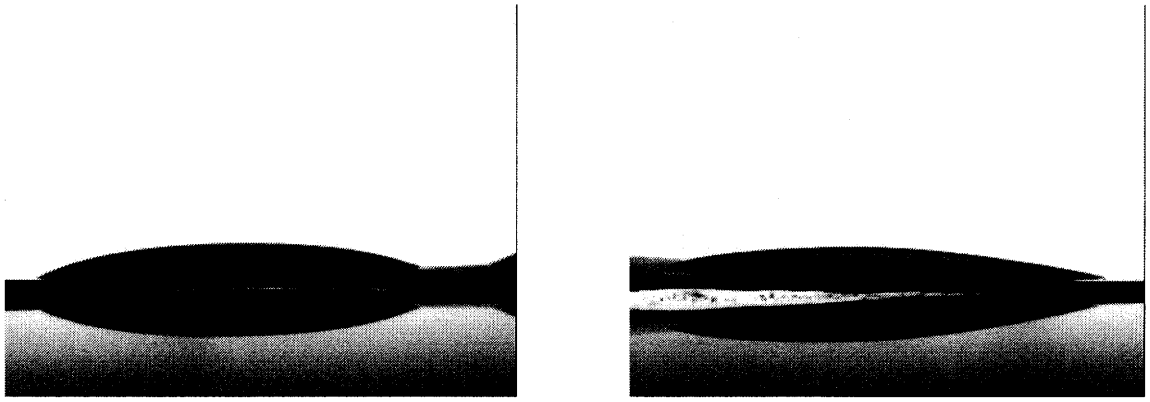

(a) 16.7° (b) 11.7°

Figure 3-12 Contact angle of 0.001 v% of $Al_2O_3$ on the flat heater boiled in the 0.001 v% $Al_2O_3$

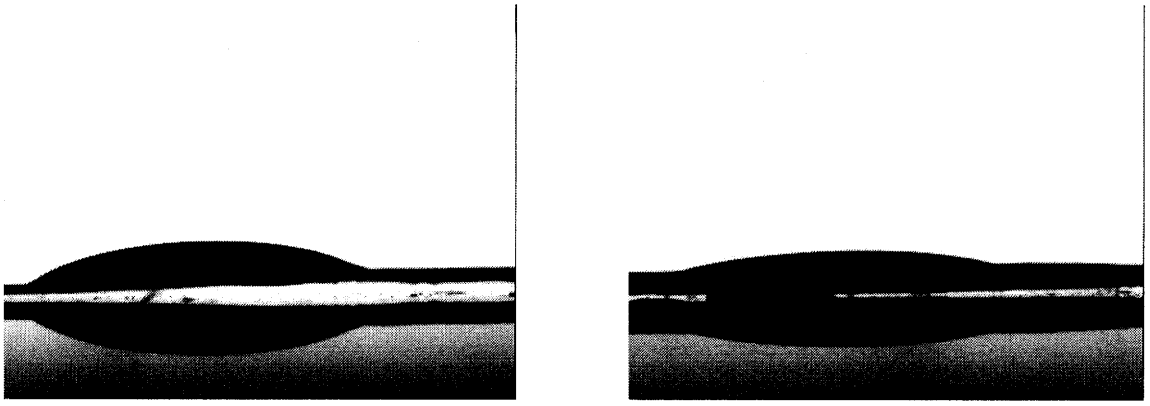

(a) 34° (b) 25.5°

Figure 3-13 Contact angle of 0.1 v% of $ZrO_2$ on the flat heater boiled in the 0.1 v% $ZrO_2$

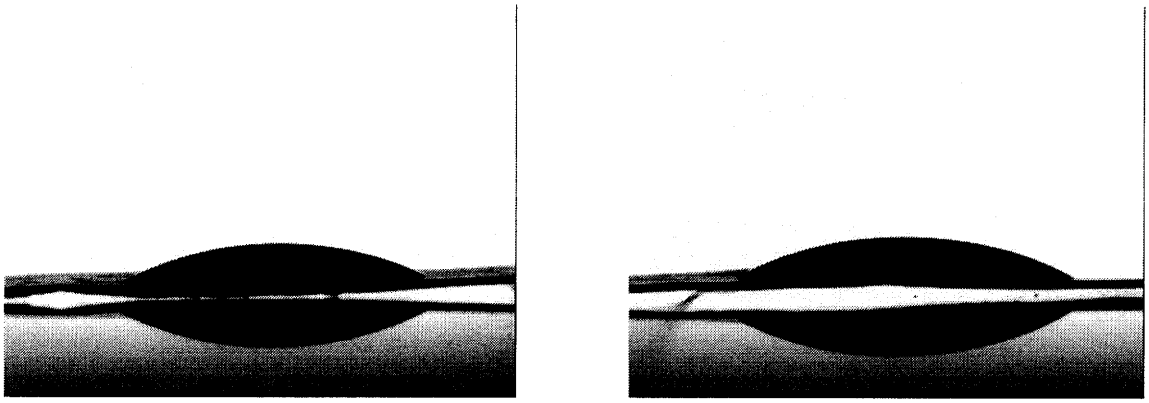

(a) 26.8° (b) 25°

Figure 3-14 Contact angle of 0.01 v% of $ZrO_2$ on the flat heater boiled in the 0.01 v% $ZrO_2$

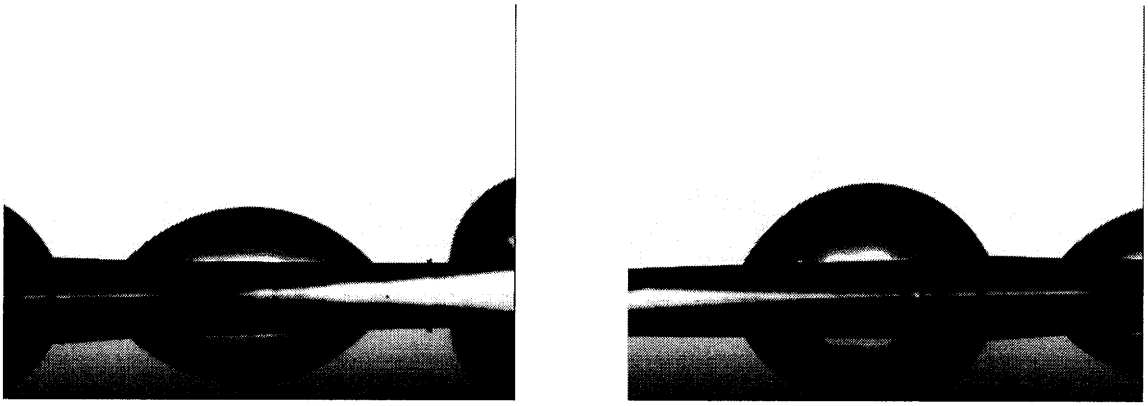

(a) 38.8° (b) 48°

Figure 3-15 Contact angle of 0.001 v% of $ZrO_2$ on the flat heater boiled in the 0.001 v% $ZrO_2$

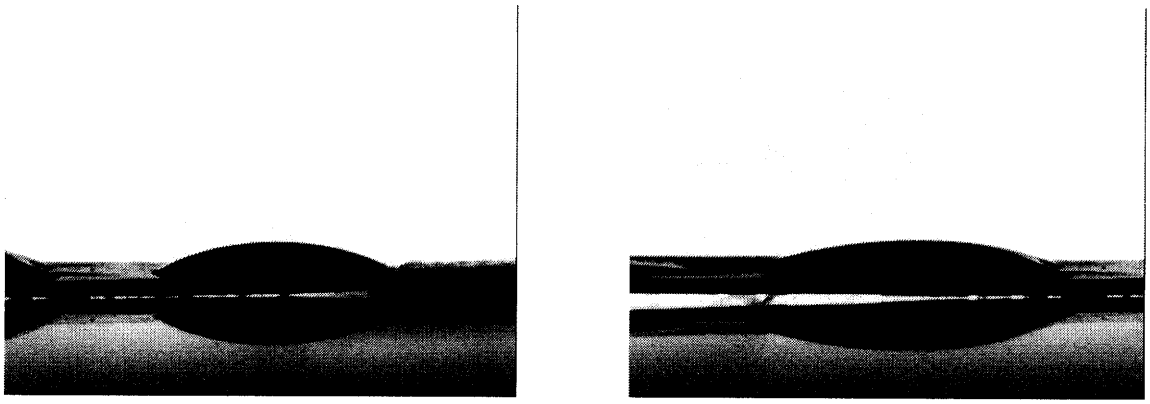

(a) 21.6° (b) 20°

Figure 3-16 Contact angle of 0.1 v% of $SiO_2$ on the flat heater boiled in the 0.1 v% $SiO_2$

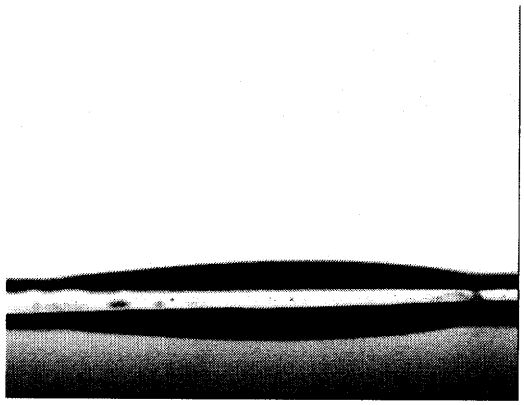

(a) 5.2°

Figure 3-17 Contact angle of 0.01 v% of $SiO_2$ on the flat heater boiled in the 0.01 v% $SiO_2$

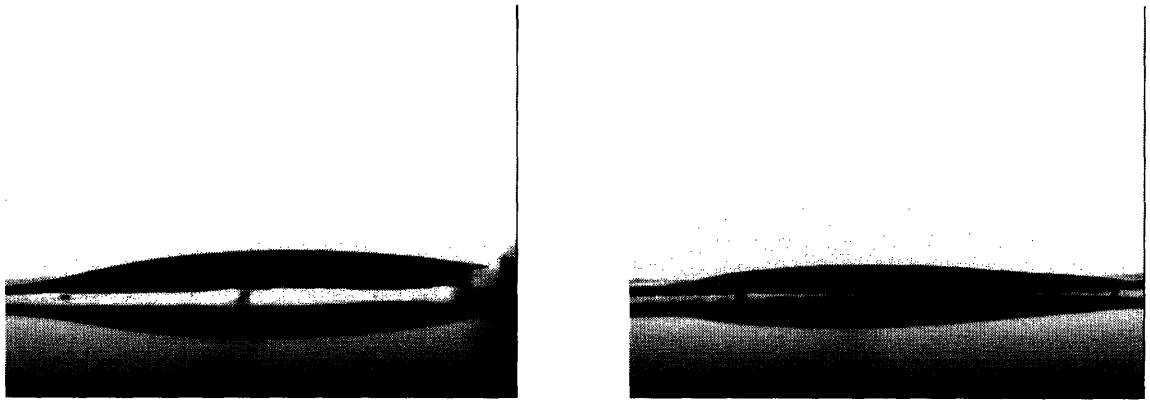

(a) 12.5° (b) 8.7°

Figure 3-18 Contact angle of 0.01 v% of $SiO_2$ on the flat heater boiled in the 0.01 v% $SiO_2$

### 3.2.3 Scanning Electron Microscopy Results

The metal surfaces of stainless steel 316 were prepared and boiled in the nanofluids such as alumina, zirconia, and silica dispersed in water. The SEM and EDS analyses again reveal that some nanoparticles precipitate on the heater surface and form irregular porous structures, which do not appear during boiling of DI water (Figs. 3-19 through 29). Therefore, with this measurement it is confirmed that morphology of the metal surface is altered by the precipitation of the nanoparticles. When the surface experiences a vigorous boiling condition, the degree of the precipitation becomes more pronounced. This is of significance because nucleate boiling heat transfer is highly affected by the surface configuration. For example, the nucleation site density can change and thus lead to either degradation or enhancement of the nucleate boiling heat transfer coefficient. On the other hand, the nanoparticle layer can alter the wettability, thus affecting CHF significantly. As mentioned earlier, the change of wettability can be quantified by measuring the change of contact angle.

According to the SEM and EDS results, some clear differences in the morphology of the nanoparticle deposition layer are evident among the various nanofluids, as shown in Figs. 3-19 through 3-29. Such differences may depend on the kind of nanoparticles contained in the nanofluids. These differences result in changes of surface energy and/or roughness of the solid surface, which in turn affect the contact angle, as will be explained in Section 4....

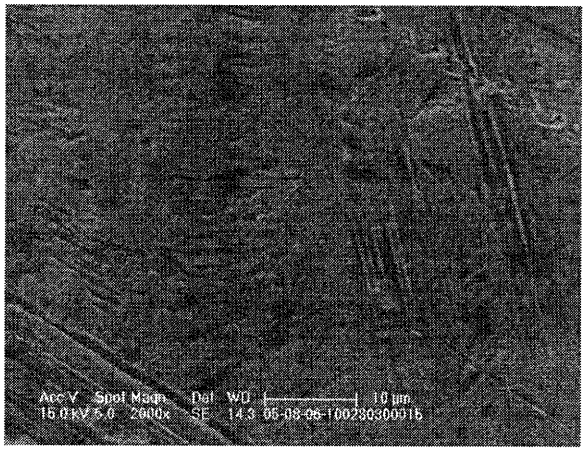


Figure 3-19 SEM picture of bare flat heater before boiling

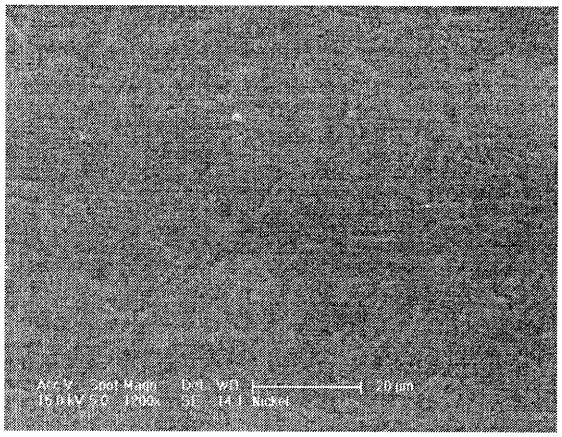


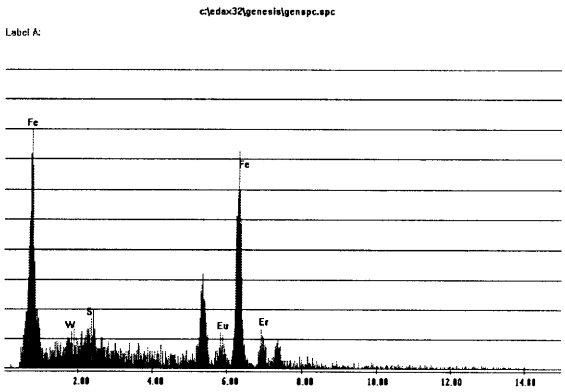


Figure 3-20 SEM picture and EDS spectrum of flat heater boiled in the DI water

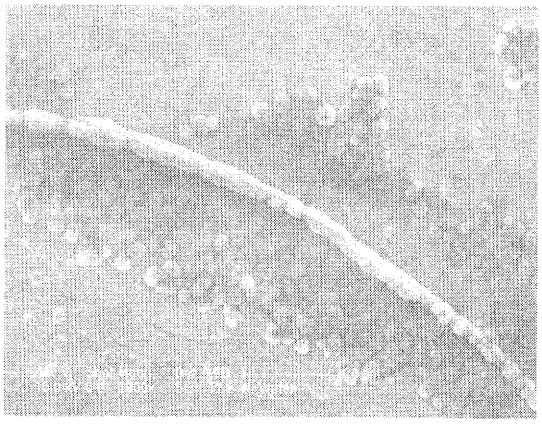

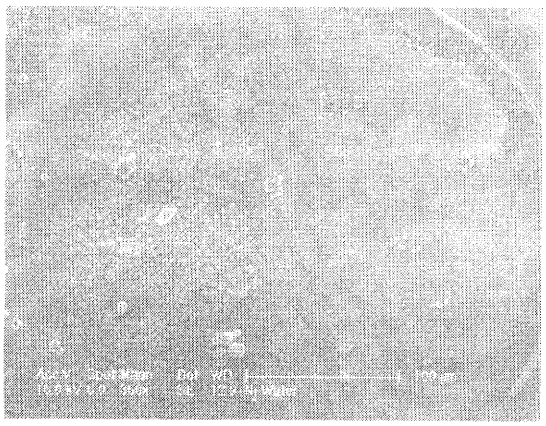

Figure 3-21 SEM picture of flat heater boiled in the 0.1 v% $Al_2O_3$

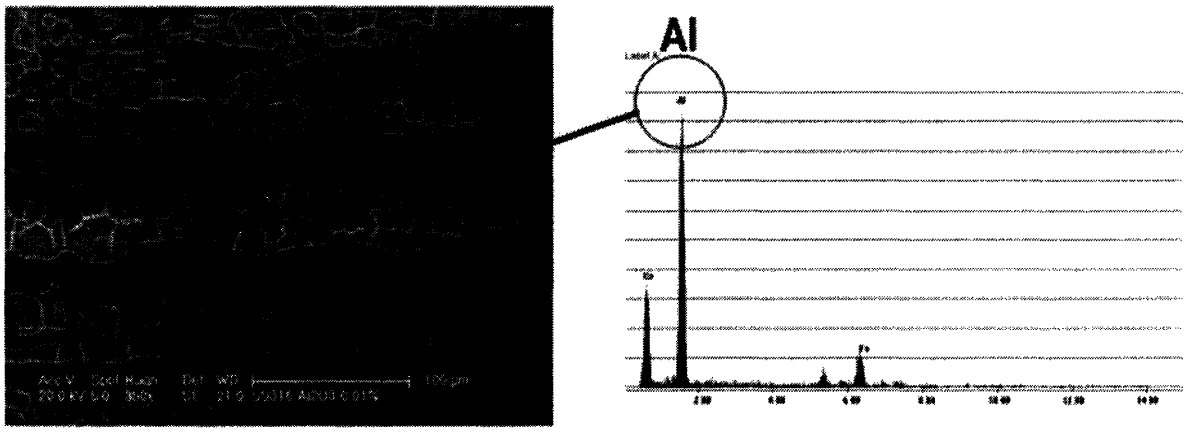


Figure 3-22 SEM picture and EDS spectrum of flat heater boiled in the 0.01 v% $Al_2O_3$

Figure 3-23 SEM picture of flat heater boiled in the 0.001 v% $Al_2O_3$

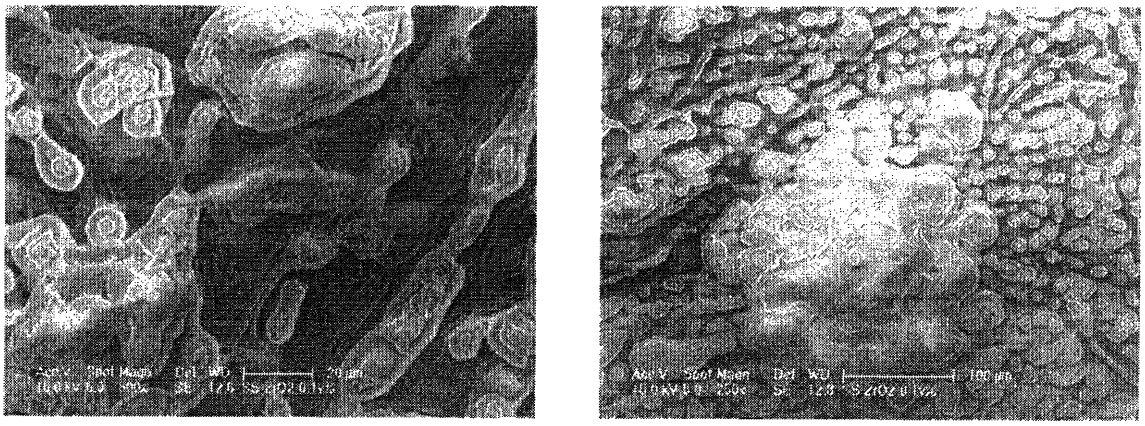

Figure 3-24 SEM picture of flat heater boiled in the 0.1 v% $ZrO_2$

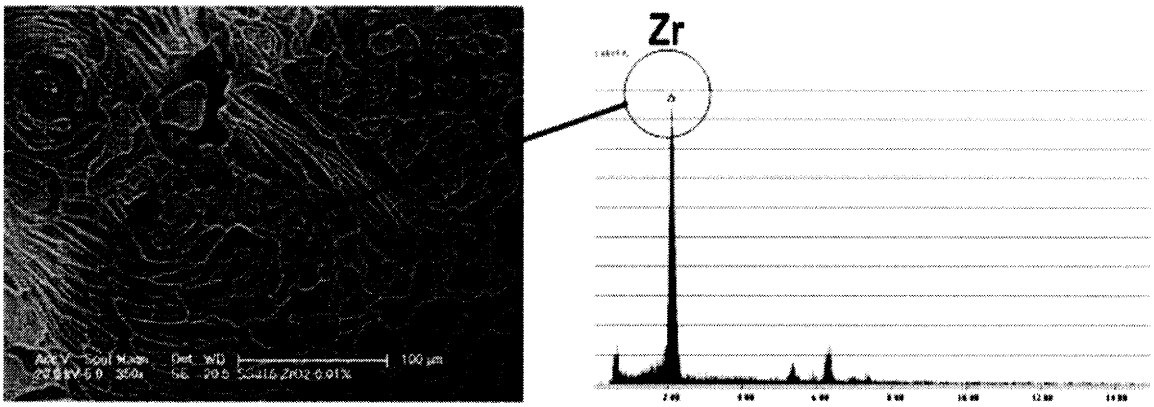


Figure 3-25 SEM picture and EDS spectrum of flat heater boiled in the 0.01 v% $ZrO_2$

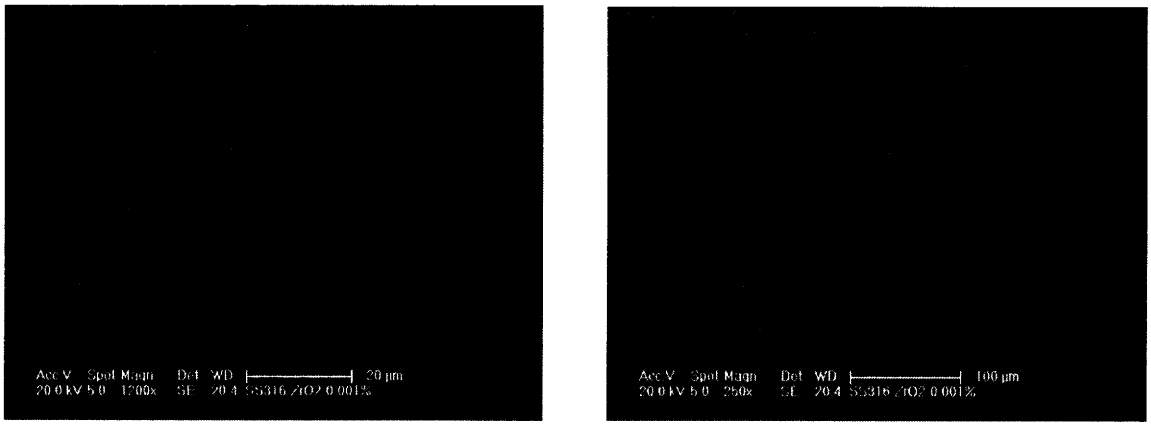

Figure 3-26 SEM picture of flat heater boiled in the 0.001 v% $ZrO_2$

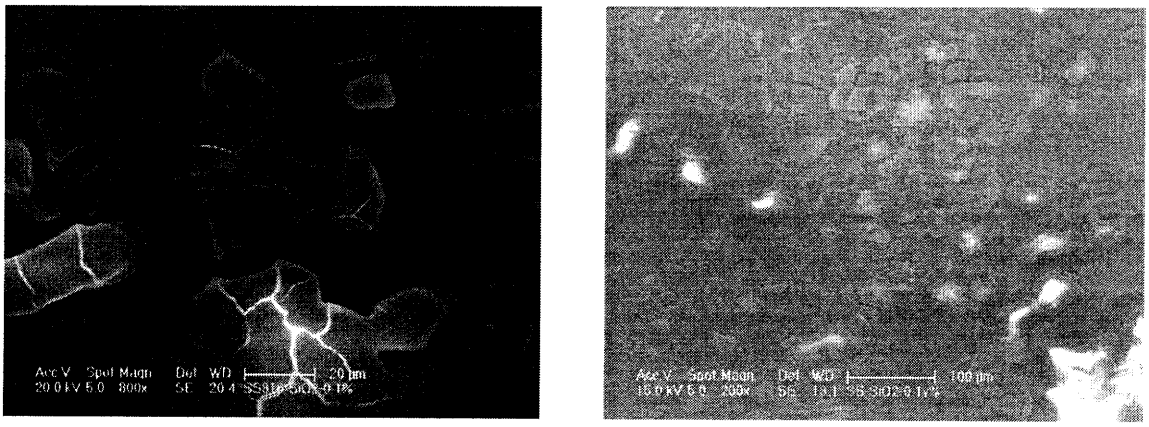

Figure 3-27 SEM picture of flat heater boiled in the 0.1 v% $SiO_2$

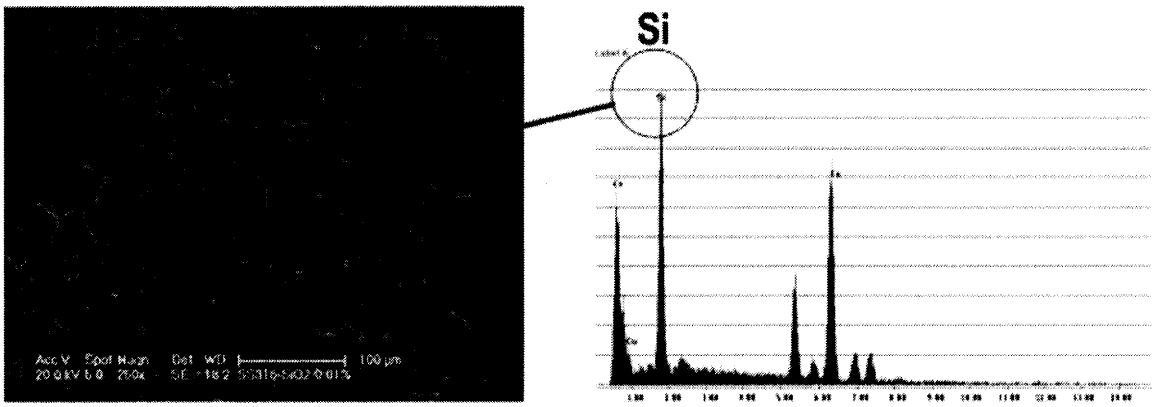


Figure 3-28 SEM picture and EDS spectrum of flat heater boiled in the 0.01 v% $SiO_2$

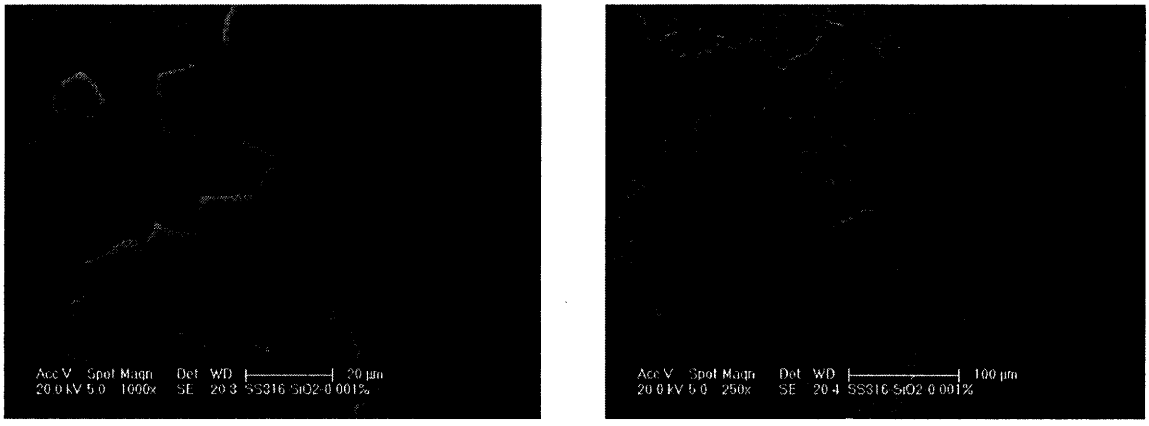

Figure 3-29 SEM picture of flat heater boiled in the 0.001 v% $SiO_2$

### 3.2.4 Surface Profilometer Results

The porous layer was analyzed more quantitatively with a Tencor P-10 surface profilometer, which gave the images shown in Fig. 3-30. The P-10 is a stylus profilometer, which uses a sharp stylus (2 μm tip radius) to quantitatively measure surface topography. The stylus is held at a fixed position, and the sample is scanned on a precision translation stage to do the measurement. This system is very commonly used for measuring the thickness of thin films using a patterned step, wafer bow for film stress analysis, and for quantitative surface roughness across large areas.

The surface boiled in DI water is very smooth, while the surface boiled in the nanofluid presents irregular peak-and-valley structures, which are consistent with the SEM images of Fig. 3-5 and 3-19 to 3-29. The roughness and total area of the surface boiled in nanofluid are about twenty times and five times higher than those of the surface boiled in DI water, respectively. The effects of such changes on the contact angle are discussed in the next section.

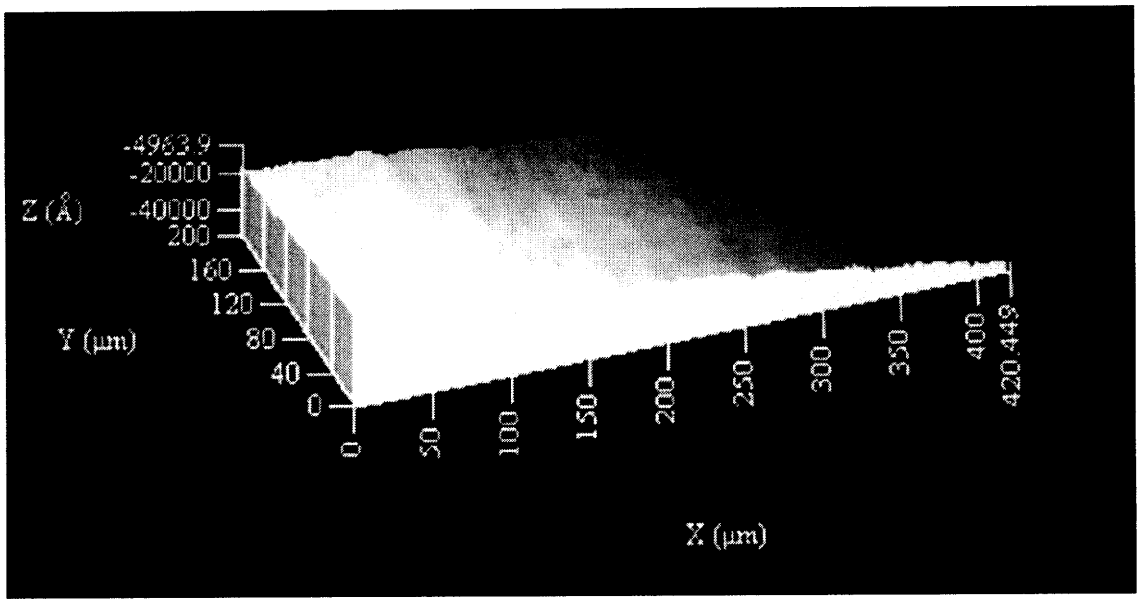
-4963.9
-20000
Z (Å)
-40000
200
160
120
Y (µm)
80
40
0
0
50
100
150
200
250
300
350
400
420.449
X (µm)

(a)

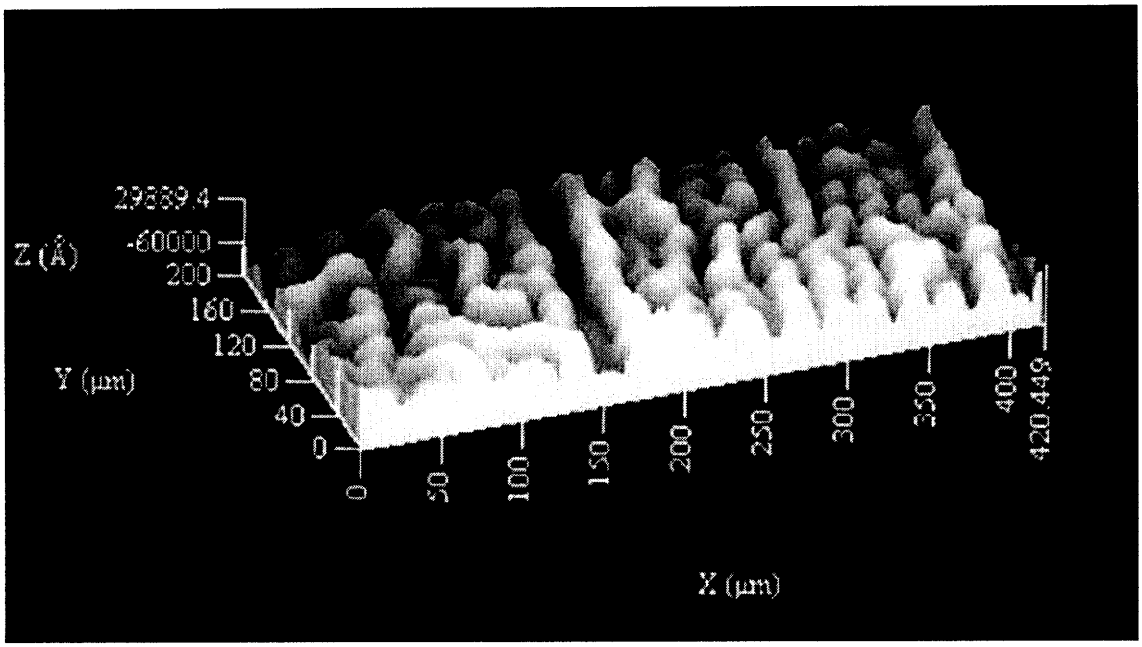
29389.4
-60000
Z (Å)
200
160
120
Y (µm)
80
40
0
0
50
100
150
200
250
300
350
400
420.449
X (µm)

(b)

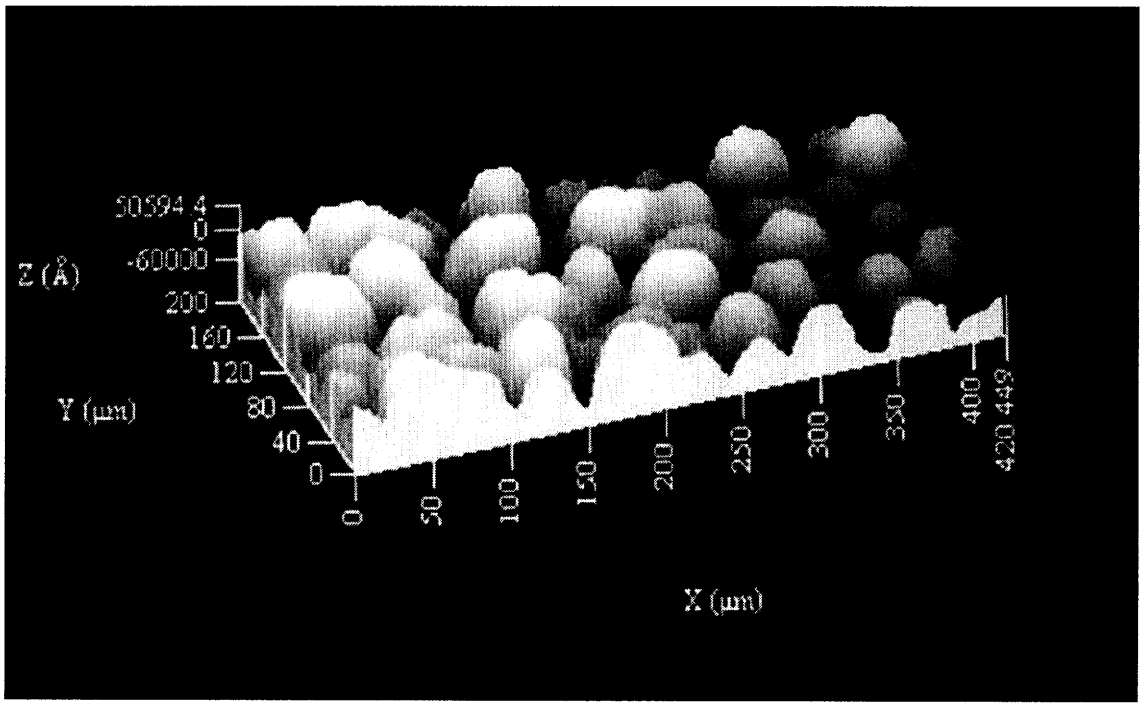


(c)

Figure 3-30 Profilometer images of the flat heater surface after boiling (a) DI water, (b) 0.01 v% alumina nanofluid and (c) 0.01 v% zirconia nanofluid. The RMS roughness values are ~0.1 and ~2 μm, respectively. Similar results were obtained with the other nanofluids.

# 4 DATA INTERPRETATION

The experiments presented in the previous Section 3 have shown that nanofluids exhibit enhanced CHF at low nanoparticle concentrations. During nanofluid boiling the heater surface becomes coated with a porous layer of nanoparticles, and such layer significantly increases surface wettability. Some questions related to the above observations naturally arise:

1) Why do nanoparticles deposit on the surface during nucleate boiling?
2) Why does the nanoparticle layer enhance wettability?
3) What effect does the nanoparticle layer have on CHF?

Questions 1 and 3 have been discussed in some detail in a separate paper [35], and only the essential conclusions are reported here. Briefly, no significant deposition of nanoparticles was observed while handling nanofluids or measuring their properties or even in single-phase convective heat transfer experiments, which are being run at MIT. Thus, it is concluded that nanoparticle deposition is a direct consequence of nucleate boiling. It is well known that a thin liquid microlayer develops underneath a vapor bubble growing at a solid surface [20]. Therefore, it is postulated that microlayer evaporation with subsequent settlement of the nanoparticles initially contained in it could be the reason for the formation of the porous layer. In ref. [35] it is shown that the layer growth rate predicted on the basis of this hypothesis is consistent with the layer thickness and experiment duration observed in our experiments. As far as the link between wettability and CHF enhancement is concerned (Question 3), most CHF mechanisms proposed in the literature, e.g., liquid macrolayer dryout [26,27] and hot spot

expansion [29-31], suggest that an increase in surface wettability will delay CHF. A semi-quantitative assessment of such effect was conducted in ref. [35] and it was found that the magnitude of the CHF enhancements reported in Fig. 3-2 is consistent with the magnitude of the contact angle reduction reported in Table 8. Therefore, it would seem plausible to conclude that the nanoparticles do affect CHF via a change in wettability of the boiling surface.

As part of this thesis work, the mechanism of wettability improvement (Question 2) was analyzed carefully. To that end, Young's equation is introduced,

$$\cos\theta = \frac{\gamma_{SV} - \gamma_{SL}}{\sigma} \tag{4-3}$$

which relates the static contact angle to the surface tension, $\sigma$, and the so-called adhesion tension, $\gamma_{SV}$-$\gamma_{SL}$. The adhesion tension of water on clean steel is ~10 mN/m and its surface tension is ~72 mN/m, so Young's equation yields a contact angle of about 82°, which is in good agreement with the measured angle of 79° (Fig. 3-9a). If the surface is not smooth, the effective solid-liquid contact area differs from the smooth contact area. Wenzel [22] defines a roughness factor, r, as the ratio of the effective contact area to the smooth contact area. The free energy of the solid-liquid interface on a rough surface is then r times the free energy of a perfectly smooth surface with the same apparent contact area. Therefore, Young's equation needs to be modified as follows [22]:

$$\cos\theta = \frac{\gamma_{SV} - \gamma_{SL}}{\sigma} r \qquad (4\text{-}4)$$

Equation (4-4) suggests that the contact angle on a rough surface depends on three parameters, i.e., the surface tension, the adhesion tension and the roughness factor. The surface tension of nanofluids tested in the current study was found to minimally differ from that of pure water (Table 4 and Fig. 2-3). On the other hand the adhesion tension of water increases significantly in going from a clean metal to an oxide, e.g., from ~10 mN/m (stainless steel) to ~60 mN/m (alumina). Such change in adhesion tension alone reduces the contact angle to ~34°, as calculated from Eq. (4-4) assuming r=1. This is consistent with other studies showing that surface oxidation decreases the contact angle [23]. The porous layer also increases the effective contact area. Thus the roughness factor, r, is greater than unity, which also contributes to the contact angle reduction in this study. To evaluate r, it is necessary to use the information obtained with the profilometer. For the situation of Fig. 3-30 (a) and (b) the estimated surface areas are about 84,000 $\mu m^2$ (clean surface) and 470,000 $\mu m^2$ (alumina-fouled surface), respectively, resulting in r~5.6. For r~5.6 the contact angle decreases to ~39°, as calculated from Eq. (4-4) with nominal adhesion tension (~10 mN/m) and surface tension (~72 mN/m). In summary, a simple analysis of the modified Young's equation suggests that the enhancement in wettability (decrease in contact angle) is caused by a combination of two effects, i.e. an increase of adhesion tension and an increase of surface roughness. Both effects are at work and large enough to cause a pronounced reduction of the contact angle.

# 5 CONCLUSION AND FUTURE WORK

The pool boiling characteristics of three water-based nanofluids (silica, alumina and zirconia) were studied experimentally. The main findings are as follows.

- Transport and thermodynamic properties of the low concentrations of nanoparticles dispersed in water differ negligibly from those of DI water.
- Dilute dispersions of alumina, zirconia and silica nanoparticles in water exhibit significant CHF enhancement in boiling experiments with wire heaters, up to 52 % for alumina, 80 % for silica and up to 75 % for zirconia.
- During nucleate boiling some nanoparticles deposit on the heater surface to form a porous layer.
- This layer improves the wettability of the surface considerably, as measured by a marked reduction of the static contact angle. The wettability improvement is due to a change in surface energy and roughness.

The first three findings are in agreement with other results previously reported in the nanofluid literature. However, it is believed that this study provides an important new clue in understanding the mechanism of CHF enhancement in nanofluids, i.e., surface wettability changes caused by nanoparticle deposition. To elucidate such mechanism more definitively, additional work is needed, including a thorough characterization of the layer growth during boiling and direct measurement of the time-dependent temperature distribution on the heater

surface, which will shed light upon the effect of the porous layer on the nucleation site density and dynamics. This should be tested in the future in order to expand the existing knowledge base. It is also necessary to resolve the discrepancy between opposite results on the nucleate boiling heat transfer coefficient.

## References


[1] S. Choi , 1995, "Enhancing thermal conductivity of fluids with nanoparticles", in *Developments and Applications of Non-newtonian Flows*, D.A. Siginer and H.P. Wang (Eds.), ASME, FED-Vol. 231/MD-Vol. **66**, pp. 99-105.

[2] J. Buongiorno and L.-W. Hu, 2005, "Nanofluid Coolants for Advanced Nuclear Power Plants", Paper 5705, *Proceedings of ICAPP '05*, Seoul, Korea, May 15-19.

[3] J. Buongiorno, L. W. Hu, S. J. Kim, R. Hannink. B. Truong, E. Forrest, "Use of nanofluids for enhanced economics and safety of nuclear reactors", *COE-INES International Symposium, INES-2*, Yokohama, Japan, November 26-30.

[4] S. M. You, J. Kim, K. H. Kim, 2003, "Effect of nanoparticles on critical heat flux of water in pool boiling heat transfer", *Applied Physics Letters*, Vol. **83**, No. *16*, pp. 3374-3376.

[5] S. Das, N. Putra, W. Roetzel, 2003, "Pool boiling characteristics of nano-fluids", *Int. J. of Heat and Mass Transfer*, Vol. **46**, pp. 851-862.

[6] P. Vassallo, R. Kumar, S. D'Amico, 2004, "Pool boiling heat transfer experiments in silica-water nano-fluids", *Int. J. of Heat and Mass Transfer*, Vol. **47**, pp. 407-411.

[7] T. N. Dinh, J. P. Thu, T. G. Theofanous, 2004, "Burnout in high heat flux boiling: the hydrodynamic and physico-chemical factors", *42nd AIAA Aerospace Sciences Meeting and Exhibit*, Reno, NV, USA, January 5-6.

[8] J. H. Kim, K. H. Kim, S. M. You, 2004, "Pool boiling heat transfer in saturated nanofluids", *Proceedings of IMECE 2004*, Anaheim, CA, USA, November 13-19.

[9] G. Moreno Jr., S. Oldenburg, S. M. You, J. H. Kim, 2005, "Pool boiling heat transfer of alumina-water, zinc oxide-water and alumina-water ethylene glycol nanofluids", *Proceedings of HT2005*, San Francisco, CA, USA, July 17-22.

[10] I. C. Bang and S. H. Chang, 2005, "Boiling heat transfer performance and phenomena of $Al_2O_3$-water nano-fluids from a plain surface in a pool", *Int. J. of Heat and Mass Transfer*, Vol. **48**, pp. 2407-2419.

[11] D. Milanova and R. Kumar, 2005, "Role of ions in pool boiling heat transfer of pure and silica nanofluids", *Applied Physics Letters*, Vol. **87**, 233107.

[12] D. Wen and Y. Ding, 2005, "Experimental investigation into the pool boiling heat transfer of aqueous based γ-alumina nanofluids", *Journal of Nanoparticle Research*, Vol. **7**, pp. 265-274.

[13] H. Kim, J. Kim, M. Kim, 2006, "Experimental study on the characteristics and mechanism of pool boiling CHF enhancement using nano-fluids", *ECI International Conference on Boiling Heat Transfer*, Spoleto, Italy, May 7-12.

[14] H. Kim, J. Kim, M. Kim, 2006, "Experimental study on CHF characteristics of water-$TiO_2$ nano-fluids", *Nuclear Engineering and Technology*, Vol. **38**, No. 1, pp. 61-68.

[15] Z. –H. Liu, Y. –H. Qiu, 2007, "Boiling heat transfer characteristics of nanofluids jet impingement on a plate", *Heat and Mass Transfer*, Vol. **43**, 699-706.

[16] K. –J. Park, D. Jung, 2007, "Enhancement of nucleate boiling heat transfer using carbon nanotubes", *Int. J. of Heat and Mass Transfer*, in press.

[17] Y. A. Çengel, M. A. Boles, 2002, *Thermodynamics, An Engineering Approach*, 4th Ed., McGraw Hill.

[18] D. Milanova, R. Kumar, S. Kuchibhatla, S. Seal, 2006, "Heat transfer behavior of oxide nanoparticles in pool boiling experiment", *Proc. of 4th International Conference on Nanochannels, Microchannels and Minichannels*, Limerick, Ireland, June 19-21.

[19] D. T. Wasan and A. D. Nikolov, 2003, "Spreading of nanofluids on solids", *Nature*, 423, 8, 156.

[20] J.G. Collier and J.R. Thome, 1996, *Convective Boiling and Condensation*, 3rd Ed., Oxford Science Publications.

[21] R. Cole and W. Rosenhow, 1969, "Correlation of bubble departure diameters for boiling of saturated liquids", *Chem. Eng. Prog. Symp. Ser.*, Vol. **65**, No. 92, pp. 211-213.

[22] R. N. Wenzel, 1949, "Surface roughness and contact angle (letter)", *J. Physical Colloid Chemistry*, **53**, 9, 1466.

[23] C. H. Wang and V. K. Dhir, 1993, "Effect of surface wettability on active nucleation site density during pool boiling of water on a vertical surface", *J. Heat Transfer*, Vol. **115**, pp. 659-669.

[24] S. S. Kutateladze, 1952, "Heat Transfer in Condensation and Boiling", *AEC-TR-3770.*

[25] N. Zuber, 1959, "Hydrodynamic Aspects of Boiling Heat Transfer", *AECU-4439.*

[26] Y. Haramura and Y. Katto, 1983, "A new hydrodynamic model of CHF applicable widely to both pool and forced convection boiling on submerged bodies in saturated liquids", *Int. J. of Heat and Mass Transfer*, Vol. **26**, pp. 389-399.

[27] P. Sadasivan, P. R. Chappidi, C. Unal, and R. A. Nelson, 1992, "Possible Mechanisms of Macrolayer Formation", *Pool and External Flow Boiling (ASME 1992)* p. 135.

[28] Y. Katto and S. Yokoya, 1968, "Principal mechanism of boiling crisis in pool boiling", *Int. J. Heat Mass Transfer*, Vol. **11**, pp. 993-1002.

[29] T. G. Theofanous et al., 2002, "The boiling crisis phenomenon. Part II: dryout dynamics and burnout", *Experimental Thermal and Fluid Science*, Vol. **26**, pp. 793-810.

[30] M. Arik and A. Bar-Cohen, 2003, "Effusivity-based correlation of surface property effects in pool boiling CHF of dielectric liquids", *Int. J. Heat Mass Transfer*, Vol. **46**, pp. 3755-3764.

[31] T. G. Theofanous and T. N. Dinh, 2006, "High heat flux boiling and burnout as microphysical phenomena: mounting evidence and opportunities", *Multiphase Science and Technology*, Vol. **18**, No. 1, pp. 1-26.

[32] S. V. Gupta, 2004, "Capillary action in narrow and wide tubes – a unified approach", Metrologia, Vol. **41**, pp. 361-364.

[33] W. Rosenhow and P. Griffith, 1956, "Correlation of maximum heat flux data for boiling of saturated liquids", *Chem. Eng. Prog. Symp.* Ser. Vol. **52**, No. 18, pp. 47-49.

[34] N. Kolev, 2002, "How accurately can we predict nucleate boiling?", in *Multiphase Flow Dynamics 2*, Springer.

[35] S. J. Kim, I. C. Bang, J. Buongiorno, L. W. Hu, 2007, "Surface wettability change during pool boiling of nanofluids and its effect on critical heat flux", *Int. J. of Heat and Mass Transfer*, in press.

[36] B. Chu, 1991, Laser Light Scattering: Basic Principles and Practice, Academic Press, Boston.

[37] P. J. Freud, M. N. Freud, 1992, A New Approach to Particle Sizing by Dynamic Light Scattering, Microtrac. Inc.